Interrelationships between aerosol characteristics and light scattering during late-winter in an Eastern Mediterranean arid environment.

By

C. Ichoku[1*], M. O. Andreae[1], T. W. Andreae[1], F.X. Meixner[1],

G. Schebeske[1], P. Formenti[1],

W. Maenhaut[2], J. Cafmeyer[2], J. Ptasinski[2],

A. Karnieli[3], and L. Orlovsky[3].

1. Biogeochemistry Department, Max Planck Institute for Chemistry, P.O. Box 3060, 55020 Mainz, Germany.
2. University of Gent, Institute for Nuclear Sciences, Proeftuinstraat 86, B-9000 Gent, Belgium.
3. Ben Gurion University of the Negev, Sde Boker Campus 84990, Israel

* Current Address: Science Systems and Applications Inc., Climate and Radiation Branch, Code 913, NASA/GSFC, Greenbelt, Maryland 20771, USA. E-mail: ichoku@climate.gsfc.nasa.gov

ABSTRACT

An intensive field campaign involving measurement of various aerosol physical, chemical, and radiative properties was conducted at Sde Boker in the Negev Desert of Israel, from 18 February to 15 March 1997. Nephelometer measurements gave average background scattering coefficient values of about 25 Mm^{-1} at 550 nm wavelength, but strong dust events caused the value of this parameter to rise up to about 800 Mm^{-1}. Backscattering fractions did not depend on aerosol loading, and generally fell in the range of 0.1 to 0.25, comparable to values reported for marine and Arctic environments. Chemical analysis of the aerosol revealed that, in the coarse size range (2-10 μm equivalent aerodynamic diameter (EAD)), calcium (Ca) was by far the most abundant element followed by silicon (Si), both of which are indicators for mineral dust. In the fine size fraction (<2 μm EAD), sulfur (S) generally was the dominant element, except during high dust episodes when Ca and Si were again the most abundant. Furthermore, fine black carbon (BC) correlates with S, suggesting that they may have originated from the same sources or source regions. An indication of the short-term effect of aerosol loading on radiative forcing was provided by measurements of global and diffuse solar radiation, which showed that during high turbidity periods (strong dust events) almost all of the solar radiation reaching the area is scattered or absorbed.

1 INTRODUCTION

Atmospheric aerosols are believed to be prominent agents of radiative forcing and climate change [*IPCC*, 1990; *Taylor and Penner*, 1994; *Schwartz and Andreae*, 1996]. This is because they have the propensity to directly absorb and scatter solar radiation, thereby modifying the atmospheric energy balance. Aerosols also have an indirect radiative forcing effect, because increased aerosol number concentration in the pre-cloud air causes increased number concentration of cloud droplets, leading to an enhanced multiple scattering of light within clouds as well as to increased optical depth and albedo of clouds [*Twomey*, 1991].

Various quantities (such as refractive index, scattering and absorption coefficients, optical depth, albedo, and so on) are used to characterize the radiative properties of aerosols. Methods of obtaining these quantities involve either direct (ground based or airborne *in situ*) measurement at discrete locations, remote sensing, or computation from measured or known parameters. Although appreciable efforts have been made to determine these aerosol radiative properties, large uncertainties remain, due to the limited number of researchers working in this field, the vastness of the area involved (the entire globe), as well as the dynamic nature of aerosol properties. Thus, to eventually have a comprehensive understanding of the composite structure and dynamics of the global radiative effects of aerosols, it is imperative to pursue relevant research covering strategic areas of the world.

In this regard, one of the locations of interest is the Eastern Mediterranean region, which has been identified as a receptor area for radiatively active natural and anthropo-

genic aerosols originating from far and near [*Maenhaut et al.*, 1996b]. Since 1995, we have been conducting, at the site of the Jacob Blaustein Institute for Desert Research in Sde Boker, Israel, continuous measurements aimed at determining the chemical, physical, and radiative aerosol properties, under a program labeled "Aerosol Radiation and Chemistry Experiment" (ARACHNE). Under this program, intensive field campaigns of several weeks' duration, involving a greater variety of instrumentation and measurements, are also carried out.

This paper presents results of the 1997 intensive campaign (ARACHNE-97) performed at Sde Boker in February/March 1997. The measurements include aerosol scattering coefficients at three wavelengths (450, 550, and 700 nm), size distribution, chemical composition by size, as well as other essential (including meteorological) data. The interrelationships between these parameters and their products, together with observed meteorological parameters are examined. Inferences are made about the probable sources of the aerosols. Results are evaluated in the global context through a comparative analysis with similar parameters obtained from other parts of the world, as published in the literature.

2 STUDY SITE DESCRIPTION

Sde Boker (30° 51'N, 34° 47'E, 470 m asl) is located in the northern part of the Negev Desert, Israel. It is at the southern boundary of the Israeli desert transition belt which is a 50 km wide East-West belt with a steep climatic gradient characterized for ex-

ample by a decrease of mean annual rainfall from 300 mm to 200 mm over this 50 km North-South span. Sde Boker therefore receives an annual rainfall of about 200 mm, all in winter. Relative humidity (RH) is generally low during the day and very high at night almost all year round. At the time of this experiment (February/March 1997), the daytime average ambient temperature and RH were about 15 °C and 52%, respectively, while at nighttime, they were about 5 °C and 98%, respectively.

Strong wind and dust events occur in the area several times a year. The timing is not regular, but the events are more common in winter than in summer. These events usually originate from the west (Europe, North Africa, and/or the Mediterranean). They bring with them aerosols from distant sources and also generate aerosols from local sources (soils and other materials). The aerosols are therefore apt to contain a wide variety of chemical elements and compounds, including mineral dust.

3 MEASUREMENTS AND INSTRUMENTATION

The intensive field campaign under discussion took place from 18 February to 15 March 1997 (25 days). The measurements made during that period (and the corresponding instruments used) are described in the following subsections.

3.1 Aerosol scattering coefficients (TSI model 3563 Nephelometer)

Aerosol scattering coefficients were measured with a 3-wavelength integrating

nephelometer (TSI model 3563: TSI Incorporated, St. Paul, Minnesota, USA). The main features of this instrument and its performance characteristics are described in detail in *Anderson et al.* [1996]. The instrument measures both the total particle scattering coefficients σ_{sp} and the hemispherical backscattering coefficients σ_{bsp} of aerosol at 3 wavelengths: 450 nm, 550 nm, and 700 nm (each of 40 nm bandwidth). The nephelometer also has sensors to measure such other relevant parameters as the temperature, pressure, and relative humidity of the air sampled. These ancillary data are measured concurrently with the scattering coefficients. During our experiment, the nephelometer was set to record all measured values at intervals of 2 minutes.

3.2 Direct solar radiation: aerosol optical thickness (Sun photometer)

An automatic tracking combined Sun photometer/sky radiometer (CIMEL Electronique 318A) is located at the site and measures direct solar radiation at intervals of approximately 15 minutes during the day. The measurements are used to derive aerosol optical thickness (AOT or τ_a) at wavelengths of 339, 380, 441, 673, 873, and 1022 nm. Unfortunately, this instrument was out of order during the campaign period.

On the other hand, on certain days during the ARACHNE-97 campaign period, 'vertical' aircraft measurements were conducted. Among the instruments on board the aircraft was a Radiance Research nephelometer model M903 (Radiance Research, Seattle, Washington, U.S.A.), which measured scattering coefficients σ_{sp} at 545 nm wavelength only. These in situ σ_{sp} measurements were used to compute AOT. Details of the flight results will be reported in a future paper.

3.3 Aerosol number concentration (PMS PCASP-100X).

Aerosol number concentrations were measured with a PCASP (Passive Cavity Aerosol Spectrometer Probe, model PCASP-100X: Particle Measuring Systems (PMS) Inc., Boulder, Colorado, U.S.A.). The instrument measures aerosol particles in 15 size classes, covering an overall nominal diameter range of 0.1 to 3 μm, as indicated by the manufacturer. However, we calibrated the PCASP-100X using the method described by *Liu et al.* [1992] and found the actual diameter range to be shifted upward, in agreement with calibration results obtained by *Liu et al.* [1992] and *Remer et al.* [1997]. Our own calibration gave the diameter range to be 0.11-3.3 μm. During the campaign, the instrument was set to record measured particle counts at intervals of 10 seconds. The generated number concentrations are easily convertible to number and volume size distributions.

3.4 Particle dual-size segregated sampling ("Gent" SFU sampler)

Aerosol samples were collected in two different size ranges: coarse (2-10 μm equivalent aerodynamic diameter (EAD)) and fine (<2 μm EAD) for chemical analysis. Numerous studies have shown that the chemistry and sources of coarse (d > 2 μm) atmospheric particles may be quite different from those of fine (d < 2 μm) particles. Three "Gent" PM10 Stacked Filter Unit (SFU) samplers [*Maenhaut et al.*, 1994] were operated in parallel during the experiment. In all three SFU samplers, the coarse aerosol particles were collected on 8 μm pore size (Apiezon-coated) Nuclepore polycarbonate filter. For the fine particles, one of the samplers was equipped with a 0.4 μm pore size Nuclepore

polycarbonate filter, another with a 2 μm pore size Gelman TEFLO filter, and the third with a Whatman quartz fiber filter (type QMA). Hereafter, the three SFU samplers will be referred to as SNN, SNT, and SNW (denoting SFU Nuclepore/Nuclepore, SFU Nuclepore/TEFLO, and, SFU Nuclepore/Whatman, respectively). Among other objectives, the concurrent use of the three samplers was to enable the verification of the reproducibility of the particle mass (PM) measurement.

During the campaign, samples were collected with the SNN and SNT samplers for continuous periods of about 12 hours (separated into day and night), while SNW was used for 24-hour sampling periods beginning and ending in the mornings. Although these constitute relatively poor time resolution compared to other measurements, the long sampling time period is necessary to accumulate sufficient aerosol mass on the filters for the chemical analysis [*Hegg et al.*, 1996b]. The filter samples were weighed and chemically analyzed at the University of Gent, as described in section 4.5.

3.5 Particle multi-size segregated sampling (SDI sampler)

To obtain detailed mass size distributions for the atmospheric particulate elements, aerosol samples were also collected in 12 size classes (in the size range of 0.045 to about 15 μm EAD). A Small Deposit area low-pressure Impactor (SDI) [*Maenhaut et al.*, 1996a] was used for these collections. Like with the SNN and SNT samplers, separate collections were done with the SDI during the daytime and nighttime periods. The samples were analyzed in Gent for their chemical composition, as discussed below (section 4.5).

3.6 Black (or Elemental) Carbon (Aethalometer model AE-9)

Black carbon (BC) is believed to originate mainly from anthropogenic emissions since there are no known natural (biological, geological, or meteorological) sources, except perhaps natural fires. The most well known sources of BC are biomass burning (forest and savanna fires) and combustion of carbonaceous fuels. Among different types of aerosols, BC is by far the strongest absorber of solar radiation, and therefore plays a prominent role in the global radiative balance. Thus, BC concentrations were measured during the campaign.

An Aethalometer (Model AE-9: Magee Scientific Company, Berkeley, California, USA) was used to determine BC concentrations. Its principle involves measuring the optical attenuation of aerosol samples deposited on a filter and converting it to the equivalent BC mass concentration through the application of a calibration factor — BC optical absorption cross section on the filter — usually a value of 19 m^2/g at 550 nm, (e.g. *Bodhaine* [1995], *Petzold et al.* [1997]). Therefore, we refer to the values obtained as Black Carbon Equivalent (BCE) mass concentrations. BC particles are typically in the small size range (usually less than 0.3 μm diameter). The instrument was operated at an airflow rate of 2.8 L/min. To discriminate against very large aerosol particles, the air was passed through a 5 μm pore size Nuclepore filter, which was changed every 24 hours approximately. At the flow rates used, this filter removes aerosol particles of diameter 1.5 μm EAD and larger from the air stream. The BCE concentration measurements are expressed in ng/m^3, and were recorded at intervals of 10 minutes during the campaign.

3.7 Condensation Nuclei (CN) Concentration (TSI Model 3022A CNC)

Condensation Nuclei (CN) particle number concentration was measured with a TSI Model 3022A CNC (Condensation Nucleus Counter: TSI Incorporated, St. Paul, Minnesota, USA). The instrument operates by passing the CN particles (which are sub-micron aerosol particles with diameter greater than 10 nm) through butanol vapor, which condenses on them, forming droplets. It then derives the number concentration from the amount of light scattered by the droplets. The measurements were recorded at intervals of 5 minutes.

3.8 Gaseous Pollutants: CO, CO_2, SO_2 (Various gas analyzers)

Concentrations of carbon monoxide (CO), carbon dioxide (CO_2), and sulfur di-oxide (SO_2) were measured to serve as tracers for pollution. CO concentrations were measured with a Trace Analytical trace gas analyzer model RGA28V (Trace Analytical, Menlo Park, California, USA), CO_2 concentrations with a LiCor LI-6252 CO_2 Analyzer (Li-Cor, Inc., Lincoln, Nebraska, USA), and SO_2 concentrations with a Thermo Electron SO_2 analyzer model 43S (Thermo Electron Corporation, Franklin, Massachusetts, USA). The CO measurements were recorded at intervals of 3 minutes, and those of CO_2 and SO_2 at 5 minute intervals.

3.9 Meteorological measurements (Conventional Instruments)

Several meteorological measurements (including pressure, relative humidity, dry- and wet-bulb temperatures, wind direction and speed, as well as direct, diffuse, and global radiation) were obtained from the meteorological laboratory of the Solar Energy Research Center located at the site of the experiment. The measurements were made with standard equipment and recorded automatically at intervals of 10 minutes. The meteorological instruments are located at about 400 m to the north of the location of the other instruments described in the preceding sub-sections.

In addition, 3-dimensional 5-day air-mass back trajectory data for Sde Boker were obtained from the German Weather Service. These data are used to infer the source areas of the mineral dust and of the pollutants.

4 DATA PROCESSING METHODOLOGY

All data were first inspected to ensure that they were free of gross errors and/or contamination. Then, certain measurements were used to derive other essential parameters as discussed below. Time averaging was applied to data sets recorded at higher frequencies (the nephelometer, PCASP, and some other data) to reduce them to 10-minute averages, corresponding to the times of the BCE concentration and meteorological measurements. This is to facilitate comparative analysis of the time series of the various data sets and their products.

4.1 Aerosol Scattering Coefficients

One of the main radiative properties of aerosols is light scattering. This is often quantified directly by means of scattering coefficients σ_{sp} and σ_{bsp}, as measured with the nephelometer. Owing to the hygroscopic and deliquescent properties of certain chemical compounds constituting aerosols, σ_{sp} and σ_{bsp} values are affected by the relative humidity (RH) of the air. This RH effect could be eliminated by applying a simple adjustment, of which the most commonly employed is that proposed by *Hänel* [1976] (see also *Hegg et al.* [1996a, 1996b] and *Remer et al.* [1997]). However, due to the internal heating of the nephelometer, the RH of the air sample inside it, as recorded by its RH sensor, was always low (mostly in the range of 30% to 60%) throughout the campaign period. This range of RH is comparable to the 50% RH value at which the SFU samples were weighed for particulate mass, as discussed below. Therefore, it was considered unnecessary to apply RH correction to the σ_{sp} and σ_{bsp} measurements.

Certain other important aerosol optical parameters have been derived from aerosol scattering coefficients. Aerosol backscattered fraction (or backscatter-to-total scatter ratio) $\beta=\sigma_{bsp}/\sigma_{sp}$ was derived for the three nephelometer wavelengths (450, 550, and 700 nm). The ratios give a rough idea about the angular dependence of scattering. Such angular dependence is generally represented by aerosol phase function $p(\theta)$ [*d'Almeida*, 1987], but the latter was not directly determined in this work. However, since β is a measure of the fraction of the scattered radiation that goes back into space, it is very useful for describing the cooling effect of aerosol on climate [*Sagan and Pollack*, 1967; *Wiscombe and Grams*, 1976].

Also derived from the scattering coefficients was the Ångstrom exponent α, which is generally computed as follows [e.g. *Heintzenberg and Charlson*, 1996]:

$$\alpha = \frac{d \ln \sigma_{sp}}{d \ln \lambda}$$

Equation 1

Where, ln designates natural logarithm, and λ = wavelength. α describes the wavelength dependence of scattering. The value of α gives a rough indication of the aerosol particle size distribution; with small values (<1) indicating a high concentration of coarse particles [*Nagel et al.*, 1998].

4.2 Aerosol Absorption Coefficients

Absorption is one of the two attenuating effects of aerosols on solar radiation (the other being scattering). Aerosol absorption is strongly related to the aerosol BC content; in fact, BC is considered to be almost exclusively responsible for all light absorption by fine particles [see *Horvath*, 1993], although absorption by large dust particles (diameter ~ 16 μm) is significant [e.g. *Tegen and Lacis*, 1996 and *Tegen et al.*, 1996]. Absorption by BC occurs over a broad range of wavelengths, and, within the visible region, it is only slightly dependent on wavelength.

Aerosol absorption (like scattering) is usually quantified by means of the particle absorption coefficient σ_{ap}. This can be either measured directly or computed from measurements of other quantities. In the latter case, one of the most widely employed tech-

niques is computation from aethalometer BCE measurements, in view of the strong relationship between BC concentrations and σ_{ap}, and since aethalometer BCE data are in fact based on optical absorption measurements (*Hansen et al.* [1984], *Bodhaine* [1995]). This method has been used in this work.

Hansen et al. [1984] originally proposed the computation of σ_{ap} from the following simple relationship:

$$\sigma_{ap} = S_{ap} B$$ **Equation 2**

where S_{ap} = specific absorption cross-section in the atmosphere (usually approximated with a constant value 10 m^2/g at λ=550 nm), and B is the BCE (in g/m^3) measured by the aethalometer. The computed σ_{ap} is therefore in units of m^{-1}. However, *Bodhaine* [1995] proposed a formula for computing σ_{ap} directly from the primary aethalometer measurements (from which it computes BCE automatically). This is given by:

$$\sigma_{ap}(550nm) = -\frac{1}{1.9}\frac{A\ln(I_2/I_1)}{Q(t_2 - t_1)}$$ **Equation 3**

where A (= 0.95 cm^2, expressed in m^2) is the aerosol collecting spot area of the aethalometer sampling filter; I_1 and I_2 are the ratios of the intensities of the sample beam to the

reference beam at times t_1 and t_2 (seconds), respectively (detector dark current measurements are subtracted from corresponding sample and reference beam detector outputs before the computation of I_1 and I_2); Q (m^3/s) is the volume flow rate of air through the sampling filter. *Bodhaine* [1995] suggested several potential advantages of Equation (3) over Equation (2). Furthermore, based on the consideration that σ_{ap} decreases with increasing wavelength, the author suggested that instead of using the constant denominator 1.9 always, the values 1.5, 1.9, and 2.4 should be used respectively at 450, 550, and 700 nm, corresponding to the wavebands of the TSI-3563 nephelometer. In this work, σ_{ap} was computed from equation (3) using the foregoing numerical constants.

4.3 Aerosol Single Scattering Albedo

The single scattering albedo ω represents the proportion of the scattered radiation out of the total energy subjected to optical extinction (scattering plus absorption). It is computed as follows:

$$\omega = \frac{\sigma_{sp}}{\sigma_{sp} + \sigma_{ap}}$$

Equation 4

In this work, ω was computed from σ_{sp} measured with the nephelometer, and σ_{ap} computed from aethalometer measurements.

4.4 Aerosol Size Distribution

Most optical properties of aerosols are dependent on aerosol particle size distribution. Size distribution data are directly derivable from the PCASP aerosol number concentration as well as the SDI mass concentration measurements described above. Whereas number concentration enables the computation of number size distribution, mass concentration yields mass size distribution.

Number size distribution can be used to simulate aerosol scattering coefficients based on the following commonly used integral relationship [e.g. *Anderson et al.*, 1996]:

$$\sigma_{sp} = \int_{D=0}^{\infty} Q_s(\lambda, m, D).\frac{\pi D^2}{4}.\frac{dN}{d\log D} d\log D \qquad \textbf{Equation 5}$$

where, N is the number concentration (such as can be obtained with the PCASP) of particles of diameter D, $dN/dlog\ D$ is the particle number size distribution, and Q_s is the dimensionless single particle scattering efficiency computed from Mie theory [*Mie*, 1908] based on the assumption that aerosol particles are spherical in shape. Q_s depends on wavelength λ, aerosol complex refractive index m, and particle diameter D.

To enable comparison with nephelometer measurements, aerosol scattering coefficients were simulated (also at 450, 550, and 700 nm wavelengths) from the PCASP number concentrations. For complete representation of the full atmospheric aerosol size spectra in the simulated scattering coefficients, the formulation (5) should be integrated over the full diameter range of aerosols (0 to ∞). Aerosol diameters generally are in the

range of 0.01 to 100 μm [*Wendisch and von Hoyningen-Huene*, 1994]. But most published works on aerosol optics consider mainly aerosols in the size range of 0.1 to 20 μm in diameter, which *Patterson et al.* [1977] identified as "the size range of the optically important atmospheric aerosols". However, the integration performed in this work only covered the diameter range of 0.11 to 3.3 μm, which was the measuring range of the PCASP.

In this work, Q_s was computed using the Mie algorithm of *Bohren and Huffman* [1983, p479]. The computation requires the user to introduce both the complex refractive index of the aerosol and the real part of the refractive index of the surrounding medium (which in this case is unity since the medium is air).

Refractive index m is usually expressed in the complex form $m=n_{Re}-n_{Im}i$, with n_{Re} representing the real part, and n_{Im} the imaginary part, where i is the indicator of the imaginary component. Whereas n_{Re} represents the ratio of the speed of light in vacuum to the speed of light in the material it describes, n_{Im} represents the light absorption capacity of the material [*Patterson et al.*, 1977]. Therefore, m depends on the composition of the material. Since the aerosols at a given location such as our study site may be composed of both local and long-range materials in different proportions at different times, the refractive index should vary with time and wavelength. Thus, strict accuracy would require the determination of m every time it is needed, and for every applicable wavelength. Such determinations are possible through the application of radiative transfer equations such as the Kubelka-Munk theory to appropriate optical data (see *Patterson et al.* [1977] and references therein). This was not possible in our case because we did not conduct the relevant reflection measurements, as this was not of major importance in this study. It was

considered that estimates of m obtained from the literature would be adequate for our purposes.

Patterson [1981], without reference to a specific location, reports that n_{Re} for aerosols lies between 1.5 and 1.6 in the visible region of the electromagnetic spectrum ($\lambda \approx 300$-700 nm). However, a previous study by the same author [*Patterson et al.*, 1977], based on measurements conducted in different parts of the world, determined that for Saharan aerosol n_{Re} =1.558 at λ=700 nm. The imaginary part n_{Im} of desert aerosols was reported to range from ~0.02 at λ=300 nm to ~0.004 at λ=700 nm, and specifically the imaginary part of Negev desert aerosol was determined to be 0.005 at λ=700 nm [*Patterson*, 1981]. The value m=1.5-0.02i was considered by *Heintzenberg and Quenzel* [1973] to be the average complex refractive index of atmospheric aerosols. *Nakajima et al.* [1983] assumed that m=1.5-0.01i was the most appropriate value for their computations, while *Moulin et al.* [1997a, 1997b] found the value m=1.5-0.02i to be most suitable for their model inversion purposes. Since it was not obvious what value would be most suitable for our case, we performed our computations with the following values of refractive index: m=1.5-0.005i, m=1.5-0.01i, m=1.5-0.02i, m=1.55-0.005i, m=1.55-0.01i. This would give us an idea of the effects of varying refractive index on simulated σ_{sp}.

The simulated σ_{sp} values will be used as a means of examining the relationship between the PCASP and nephelometer measurements through relevant error analysis. The accuracy analysis will be discussed in the analysis section below.

4.5 Aerosol physical/chemical composition

The SNN and SNT coarse and fine filters were analyzed for particulate mass (PM), by weighing with a microbalance (with 1 μg sensitivity) at 50% relative humidity and 20°C. For the SNN filters, black carbon (BC) was then determined by a light reflectance technique [*Andreae*, 1983; *Andreae et al.*, 1984], and the same filters were also analyzed by Instrumental Neutron Activation Analysis (INAA) and Particle-Induced X-ray Emission (PIXE) spectrometry. The combination of the two techniques enabled us to measure over 40 elements. The SNW fine quartz filters (QMA) were analyzed for Organic Carbon (OC) by a thermal-optical transmission (TOT) technique (Birch and Cary, 1996), using an instrument from Sunset Lab (Forest Grove, OR, USA). The SDI samples were analyzed by PIXE (for over 20 elements). In all cases, concentrations were expressed as mass per unit volume of air at ambient temperature and pressure (usually $\mu g/m^3$ or ng/m^3). Details of the instrumentation and analytical methods are given in *Maenhaut* [1997].

The elements detected and measured with the INAA and PIXE techniques from the SFU-SNN and SDI samples include Na, S, Al, Si, K, Ca, Ti, and Fe, to mention just a few. Of these, the ones that are of greatest interest in this study are: S (as indicator for sulfate), Na (as indicator for sea salt), Ca (as indicator for carbonate mineral dust), Al, Si, Ti and/or Fe (as indicators for the alumino-silicate mineral dust). From the SFU-SNN fine and coarse concentration measurements of these elements, the main aerosol constituents (sulfates, sea salt, carbonates, and silicates) in the study area were estimated, based

on average concentrations of elements in crustal rocks and sea-water presented in *Mason and Moore* [1982, Tables 3.5 and 9.3]. The results are presented in the analysis section below.

5 RESULTS AND ANALYSES

It is worthwhile to begin by looking at the time series of certain essential measured and computed parameters covering the period of the campaign. This will provide a general picture of their state and evolution during that time period.

5.1 Time Series

Figure 1 shows time series of: (A) σ_{sp} measured with the nephelometer at 550 nm (used because 550 nm is approximately the central wavelength of the visible region, and is the most widely referenced wavelength in aerosol optics); (B) Ångstrom exponent α from σ_{sp} at 550 nm; (C) PCASP particle number concentration in the size range 1.0-3.3 μm, N_{coarse}; (D) PCASP particle number concentration in the size range 0.11-1.0 μm, N_{fine}; (E) PCASP particle volume concentration in the size range 1.0-3.30 μm, V_{coarse}; (F) PCASP particle volume concentration in the size range 0.11-1.0 μm, V_{fine} (G) backscattered fraction β at 550 nm (from the nephelometer measurements); (H) Black Carbon Equivalent (BCE) concentrations from the Aethalometer; (I) single-scattering albedo (SSA), ω; and (J, K, L, M) concentrations of CO, CO_2, SO_2, and CN, respectively. All charts in Figure 1 are plotted from the 10-minute averages of the different data sets. The

gaps in the graphs show periods when no data was acquired due to instrument (or other) problems.

The scattering coefficient σ_{sp} time series (Figure 1A) provides an insight into the optical effect of aerosol loading during the intensive campaign period. Shortly after the beginning (21 to 23 February 1997), there was a succession of high scattering events characterized by a series of peaks. This was followed by a clear period, which was succeeded by three periods of moderate turbidity separated by interludes of low turbidity. Comparison of the scattering time series with that of the particle number and volume concentration in the fine and coarse fractions provides a first, qualitative assessment of the influence of the aerosol concentration on atmospheric turbidity. The dust events show up as sharp peaks in the aerosol number and volume concentrations and in the scattering coefficient. Because large particles scatter light with approximately the same efficiency across the visible spectrum, the dust events result in minima in the Ångstrom coefficient (Figure 1B). The effect of the fine aerosol fraction is only seen in the absence of high dust loadings, particularly in the period 27 February to 3 March. During this time, the scattering is closely related to the number and volume concentrations of the fine fraction. These relationships will be more quantitatively explored in section 5.5.

As pointed out above, the Ångstrom exponent α (Figure 1B) is a function of particle size; being low for higher concentration of large particles and higher otherwise. The range of α values observed during our experiment range, –0.3 to 2.3, spans the values expected for coarse mineral dust at one extreme to fine pollution aerosol at the other. Although the backscattered fraction β (Figure 1G) shows some variation (which seems to obey a diurnal cycle), it does not appear to depend on the level of scattering, nor on parti-

cle size distribution. The pattern of β does not provide prominent features that would enable a consequential interpretation with regard to aerosol radiative forcing. However, closer observation shows that the general level of β appears to be lowest around 1 March 1997, which, as will be seen later, is the period with the highest concentration of polluting agents (as opposed to dust). It is noteworthy that β values obtained during the period of our experiment generally fall in the range of 0.1 to 0.22 (with the exception of a few outliers), which is comparable to the range 0.08 to 0.2 reported by *Hegg et al.* [1996a] for marine environments as well as 0.07 to 0.24 [*Hegg et al.*, 1996b] for the Arctic environment.

The black carbon equivalent (BCE) concentration plot (Figure 1H) shows appreciable correlation with fine particle volume concentration, as well as with other indicators of fossil-fuel derived pollution, such as CO and SO_2. This is particularly evident during the pollution episodes (1-2 and 10-12 March). In modeling aerosol radiative forcing, "the key parameter governing the amount of cooling versus heating is the single-scattering albedo ω" [*Seinfeld and Pandis*, 1997]. This parameter (Figure 1I) was computed from the absorption coefficients (derived from the aethalometer measurements) and the nephelometer-measured scattering coefficients, both at 550 nm wavelength. Periods with very high coarse particle dust concentration are not included because a pre-filter was used to exclude coarse particles from the aethalometer, and the measured values during those periods were unrealistic. Otherwise, with the exception of a few low values due probably to noise from the aethalometer measurements or to local effects, the ω values in this work fall approximately in the range of 0.76 to 0.97, with no obvious relation to either pollution or dust events. The last short segment with extremely high values may also be due to

aethalometer instrument noise, as will be seen later when the BCE is compared with the SNN-sampled BC. Our range of ω-values (0.76 to 0.97) is somewhat wider than that (0.85 to 0.96) obtained by *Hegg et al.* [1997] from vertical column measurements off the mid-Atlantic coast of the United States. Values of ω representative of various desert dust aerosol models, compiled by *Moulin et al.* [1997a, p. 16,964, Table 3] from the literature, show a range of 0.71 to 0.94.

We used the trace gases (CO, CO_2, and SO_2), the Aitken particle concentration (CN), and the black carbon concentration (BCE) as indicators for the presence and origin of anthropogenic pollution. CO and BCE are relatively long-lived species (days to weeks) related to combustion, while CN and SO_2 have lifetimes of hours to days and therefore reflect more local emissions and photochemical activity. SO_2 and CN show large peaks during the non-dusty, polluted periods such as 1 to 2 March and 10 to 12 March. In order to assess the mutual relationship between the various trace gases and CN, we calculated their correlation coefficients, r, and found them to be very low (generally in the range of -0.2 to 0.2), with the exception of SO_2 and CN between which r=0.57. This suggests that these two species are from local and regional pollution from Israel and surrounding areas, as opposed to long-range transport. Their probable origin is from power plants, industries and vehicular traffic along the Israeli coastal areas and other locations. We find that during this wintertime experiment, regional pollution played a more prominent role than during our previous summer campaign and in our long-term data set acquired at Sde Boker [*Maenhaut et al.*, 1996b, 1997].

In summary, a comparative analysis of the various time series in Figure 1 reveals two prominent aerosol regimes: dusty and polluted periods. Dusty periods are mainly

characterized by high values of scattering coefficients and large coarse aerosol number and volume concentrations, as exemplified by the cluster of peaks around 21-23 February 1997 (Figures 1A, C, E). On the other hand, polluted periods can be inferred from the peaks and temporal behaviors in the BCE, CO, SO_2, and CN time series. Two main polluted periods, namely 1-2 March and around 10-12 March 1997, are noticeable in all these parameters, as well as in fine particle number and volume concentrations.

To enable a more detailed analysis of the various data sets as well as to establish their interrelationships and closures, we shall focus in the following sections mainly on data acquired over short periods of time but under different aerosol regimes. As such, a few days will be selected for further study. This will be based on relative concentrations of mineral dust versus pollutants, as discussed in the next subsection.

5.2 Representative Days for Different Configurations of Aerosol/Pollution Levels

In making the selection of representative days, concentrations of dust will be based on coarse aerosol volume derived from the PCASP measurements, while the presence of pollution will be based on the combined concentrations of BCE, CN, CO and SO_2. During our intensive campaign, the pollutant levels (BCE, CN, CO and SO_2) are quite low during some periods (e.g., 25-26 February and 5-7 March) and reach levels typical of moderately polluted rural areas during the rest of the campaign. Nevertheless, there are quite prominent variations in the levels of concentration of both dust and pollutants with time. Based on this, we have selected for further study 5 days with different aerosol/pollution regimes, namely 21 and 26 February, and 1, 6, and 12 March 1997. The

characteristics of these days in terms of concentrations of aerosols and are listed in Table 1. All concentration values shown are averages of the measurements for the time intervals shown, all of which are one-hour periods. This one-hour averaging time period is considered a reasonable time to obtain quantities representing sustained conditions, and to avoid the use of values which could reflect an extremely short-term and unrepresentative condition.

The categorization of dust levels into *Low*, *Medium*, and *High* is based on aerosol volume. Pollution level categorization is based on CO, BCE, and (mostly) SO_2 concentration, because the latter has exhibited by far the most significant variability over time in comparison with the other species. For instance, in Table 1, the ratio between the highest and the lowest values is less than 2 for BCE and CO, about 6 for CN, about 104 for dust, but more than 1000 for SO_2. Note that we refrained from having a *High* category for pollution level because the entire period of our experiment was fairly clean, with moderate levels of regional and long-range pollution.

5.3 Simulated Scattering Coefficients

Figure 2(A and B) illustrates the comparison between the measured (nephelometer) and simulated (Mie-theory with size distributions from the PCASP) σ_{sp} at the 550 nm (green) wavelength band for two different aerosol regimes (highest dust and highest pollution). There is high (and almost equal) overall correlation between the measured and all the simulated data sets, as demonstrated by the correlation coefficients r in Table 2, which are computed from the data for the whole campaign period. During the dusty day

(21 February 1997), the deviations between these simulated values and their measured counterparts are very small (Figure 2A). This excellent agreement is somewhat surprising, considering the fact that the PCASP size distribution extends only up to 3.3 μm, and may reflect a cancellation of errors from the truncation of the measured size distribution and truncation errors resulting from the geometry of the nephelometer [*Anderson et al.*, 1996].

On the other hand, the day with the least dust and highest pollution (01 March 1997) showed a moderate deviation between simulated curves, which remained almost the same throughout, with the measured scattering coefficients higher by factors of 1.2-2 than those of the simulated data sets. The effect of the different refractive indices on the deviations is represented by the root mean square error (rmse) values in Table 2, also computed from all the campaign data. The curve with m=1.55-0.005i is closest to the measured data set (with rmse=20.2 Mm^{-1}). The observed discrepancies are probably the result of combined uncertainties in the determination of the true geometric size of the particles with the PCASP, the determination of the scattering coefficients, and the application of the Mie theory to non-ideal particles.

5.4 Aerosol size distribution

Figure 3(A, B, C, D and E) shows plots of particle number size distribution under the 5 aerosol regimes. In each case, 6 successive distributions of 10-minute averages (covering the one-hour periods shown in Table 2) have been plotted. During the very high dust event of 21 February, there is little variation in the aerosol number concentra-

tion relative to diameter. But at low dust periods, the curves present bimodal features as is typical within the measured size range (0.11 to 3.3 μm diameter), with very distinct difference in the levels of the two modes. The concentrations could be seen from a different perspective by plotting the volume size distribution (see Figures 4A, B, C, D, E), which again clearly show a bimodal distribution, except for that of 21 February (the very high dust event).

5.5 Volume scattering efficiencies

To assess quantitatively the influence of the volumes of the two particle size modes (coarse and fine) on scattering, particle volumes were computed from the PCASP measurements separately for the coarse and fine modes. Correlation analysis was performed between each of the measured scattering coefficients (both total and back, at all 3 wavelengths, 450, 550, 700 nm), and the particle volumes in the fine and coarse size modes for the entire campaign period. The correlation coefficients, *r*, are presented in Table 3. In all cases, the coarse size mode shows much higher correlation to scattering than the fine fractions. Furthermore, whereas correlation is inversely proportional to wavelength in the fine size fractions, it is directly proportional to it in the coarse mode, particularly for the total scatter. This is to be expected, because coarse particles contribute more strongly to scattering at longer wavelengths.

While the correlation coefficients in Table 3 indicate how closely the coarse and fine size volumes covary with the scattering coefficients, they do not show the relative influence of the volume of each size fraction on scattering, i.e., the volume scattering ef-

ficiencies. The latter relationship can be determined through multivariate regression analysis. A multivariate analysis was performed between the measured scattering (and backscattering) coefficients at the various wavelengths as a function of the fine and coarse particle volumes, based on linear relationships of the following form:

$$\sigma = a_0 + a_f v_f + a_c v_c$$ **Equation 6**

where, σ represents the nephelometer-measured scattering (or backscattering) coefficients at a given wavelength, a_0 is the intercept of the multivariate regression line, v_f and v_c denote, respectively, volumes of the fine and coarse fractions (from the PCASP number concentration measurements), while a_f and a_c denote their coefficients. For use in equation (6), the parameter σ is expressed in m^{-1}, the v's in cm^3/m^3, and therefore the units of the a's are m^2/cm^3. The coefficients a_f and a_c can be regarded as the volume scattering efficiencies for the fine and coarse size particles respectively. Table 4 shows the values of the coefficients a_f, and a_c (and associated standard errors) for σ_{sp} and σ_{bsp} at the three nephelometer wavelengths (450, 550, and 700 nm). It is obvious that, although the volume of the coarse size fraction gave much higher r-values than that of the fine particles, the latter influences scattering much more for a given amount of aerosol volume (since in a multivariate regression, the coefficient of an independent variable is a measure of its relative influence on the dependent variable). Again as above, the influence of the fine particle volume on scattering is seen to decrease with wavelength, while the reverse is the case for the coarse particle volume. Only the volume backscatter efficiency for the

coarse fraction shows no significant trend with wavelength. It should be noted, however, that PCASP-measured particle size ranges from which the volumes are computed are intrinsically truncated in both the fine and coarse size ranges from below and above respectively. While this has little effect on the volume of the fine mode, the mass scattering efficiencies for the coarse mode must be regarded as upper limits. A similar pattern of behavior with regard to wavelength was observed by *Maenhaut et al.* [1997] for the same area, with mass (instead of volume), using longer term data for 1996, with slightly different diameters of size range demarcation and truncation.

5.6 Aerosol Mass Concentrations and Scattering Efficiencies

Aerosol mass concentrations and their variations during the campaign period may be studied using time plots of SFU particle mass (PM) data. Since these were acquired only as daytime and nighttime data, they consist of only two data points per day. The data for coarse and fine particles are plotted separately as shown in Figure 5(A and B), but in each case, SNN and SNT data are plotted together for comparison. With minor exceptions, especially at certain sharp peaks and troughs, corresponding PM data from the two samplers (SNN and SNT) are seen to be in close agreement. Note that the scale for the coarse particles is higher than that for the fine particles by about one order of magnitude, due to the enhanced concentration of the former during dust events. To visualize graphically the time evolution of the PMs relative to scattering coefficients, coarse and fine PM measurements from the SNN are plotted alongside σ_{sp} at 550 nm averaged for the periods of acquisition of the SNN data (which, of course, also represent average values). The

composite plot (Figure 6) shows the variation of the scattering coefficients to be consistent with both particle mass concentrations.

The relative mass scattering efficiencies of the fine and coarse size fractions can, like volume scattering efficiencies, be estimated from equation (6), with v_f and v_c this time representing the mass (instead of volume) concentrations of the fine and coarse particles, respectively. Like *Maenhaut et al.* [1997], to avoid undue bias by the extreme dust event that occurred in the early hours of 21 February 1997, the data line representing that event was excluded before the computations. As above, here also the parameter σ is expressed in m^{-1}, but the v's are in g/m^3, while the a's are in m^2/g. The values of the coefficients of the equations and the associated standard errors are given in Table 5. These mass scattering efficiencies (a_f and a_c) exhibit the same pattern of behavior as their corresponding volume scattering efficiencies derived above (Table 4) and also those of the mass scattering efficiencies presented by *Maenhaut et al.* [1997]. In other words, the mass of the fine size fractions influences scattering much more than that of the coarse, and the effect of the fine mass decreases with wavelength while that of the coarse increases with it.

5.7 Aerosol Chemical Composition and Source Estimation

The contributions of individual elements to the composition of the aerosol in the study area can be appreciated from time plots of the mass concentrations of these elements obtained from the analysis of the SNN data. Figure 7(A and B) shows separate time plots for the coarse and fine particles. As previously indicated, the elements repre-

sented in these plots are the most relevant to the determination of probable aerosol sources. Thus, S is the indicator for sulfate, Na for sea salt, Ca for carbonate mineral dust, and Al, Si, Ti and/or Fe are indicators for alumino-silicate mineral dust. In the coarse size range, calcium (Ca) is the dominant element all the time, while in the fine size category, it is most abundant only during prominent dust events (e.g., on 21 February 1997) whereas sulfur (S) dominates at other times. Fine sulfur was, in fact, highest on the most polluted days (1-2 March 1997). Silicon features prominently both in the coarse and fine size modes, especially during dusty periods. These observations indicate that the bulk of the aerosols occurring during dust events (both in the coarse and fine categories) are of mineral dust origin. By contrast, sulfur concentration appears to be indifferent to dust events, and is otherwise appreciably high relative to the other elements, especially in the fine mode.

A look at the air-mass back trajectories revealed that on the dusty days, 21 February and 6 March 1997, the air masses in the lowest 1.5 km of altitude came through Eastern Europe, over the Mediterranean, then at high windspeeds through the northern parts of Egypt and the Sinai Peninsula. On 12 March 1997 the trajectories came from different directions: North Africa and the Mediterranean, the Arabian peninsula and Turkey. The low-level airmasses circulated over the coastal corridor of Israel, picking up pollution from the power plants and population centers along the coast. In contrast, 26 February 1997, which showed the lowest concentration of any of the substances during the experiment, had air masses arriving mainly from Eastern Europe/Turkey/Mediterranean, then brushing the northern coastline of the Sinai peninsula, but avoiding the coastal corridor of Israel. On the most polluted day, 1 March 1997, near-surface airmasses arrived from the

West across the Mediterranean, Egypt and the Sinai, which normally brings clean air to the site. However, they then circulated over the population centers of Israel for some time before terminating over Sde Boker. Consequently, the fact that 1 March 1997 is characterized by high concentrations of short-lived pollutants as well as fine sulfur aerosol may be due to regional pollution inputs.

Sodium is fairly noticeable in both size ranges and appears to have relatively high concentration when the air masses enter the area soon after passing over the Mediterranean. This suggests that there is a sea salt component in the aerosols over the study site during such occasions, originating from the Mediterranean.

Black carbon (BC) concentrations (coarse and fine) from the SFU are plotted in Figure 8. To enable comparison with aethalometer-BCE measurements, these were averaged over the periods of the SFU collections and plotted alongside the SFU-BC curves. Obviously, the aethalometer-BCE exhibits appreciable covariance with the fine SFU-BC (but not with the coarse SFU-BC). However, the fine SFU-BC values are consistently higher than their aethalometer-BC counterparts, perhaps due to differences in certain aspects of instrument characteristics. Adopting the SFU-BC data for further analysis, we find that the coarse size component appears to respond to dust events (in a manner not necessarily proportional to the aerosol loading), while the fine component does not (— compare with Figure 1). Note, however, that during the dust events a considerable fraction of the light absorption of the coarse aerosol may have been due to the mineral dust itself rather than to black carbon proper. Fine BC appears to be correlated with fine sulfur (— compare with Figure 7B), suggesting that they could be from a common anthropogenic source area, from which they are advected together by the same air mass. To ex-

press the foregoing relationships in a more condensed form, their mutual correlation with one another as well as with the average measured scattering coefficient at 550 nm wavelength have been computed and presented in Table 6. In this table, it is again obvious that fine BC, unlike other elements, shows an appreciably high correlation (r=0.6) with fine S. On the other hand, despite the fact that sulfates (which are responsible for virtually all of the S) are believed to be one of the principal aerosol constituents that contribute to light scattering in the unperturbed atmosphere [*Charlson et al.*, 1992], fine S in this data set is virtually uncorrelated with σ_{sp}. This lack of correlation is due to the overwhelming effect of scattering by mineral dust.

As a summary of the aerosol composition during the 5 representative days, Figure 9(A and B) shows a display of the estimated relative concentrations of the main aerosol constituents in the coarse and fine size ranges. Note that, overall, the total aerosol mass in the coarse size fraction is about an order of magnitude higher than that of the fine fraction. Nevertheless, the relationships described in the foregoing paragraphs are quite vividly portrayed in the charts. For instance, in the fine size range (Figure 9A), the 01 March 1997 shows the highest concentrations of both sulfate and black carbon.

Detailed mass size distributions of the selected individual elements have been retrieved from the SDI measurements of the concentrations of these elements (obtained by PIXE analysis). They are plotted for the five selected dates of different aerosol regimes in Figure 10(A, B, C, D, and E). Note that gaps occur in the plots in places where the PIXE technique did not give reliable mass concentration values, although this does not affect the plots significantly. Also, it should be noted specifically that PIXE measurements of Na are not very reliable because of the uncertainty in the matrix correction factor for the

attenuation of the soft Na K-alpha X-rays in the aerosol particle deposit. However, overall, only S and Na appear to show bimodal distributions, with the fine size fraction of S being more pronounced, while all other elements are mainly concentrated in the coarse size range. Moreover, except for the day with the highest dust event (21 February 1997), in each of the other cases the sulfur concentration is higher in the fine than in the coarse size range.

5.8 Aerosol Radiative Forcing

The global mean solar radiation per unit area at the mean distance of the Earth from the Sun (also known as the solar constant) is estimated to be about 1370 Wm^{-2} [*Charlson et al.*, 1992]. This value is believed to be the mean solar flux reaching the top of the atmosphere (TOA). Naturally, before the radiation reaches the earth's surface, some of it is lost in the atmosphere through the processes of scattering and absorption by natural atmospheric constituents (air, water vapor, and so on). Aerosol radiative forcing is the result of additional losses in solar radiation due to anthropogenic aerosols [*Charlson et al.*, 1992; *Kiehl and Briegleb*, 1993; *Taylor and Penner*, 1994; *Tegen et al.*, 1996; *Seinfeld and Pandis*, 1997].

The principal reason for the study of the optical properties of atmospheric aerosols is to attempt to determine their radiative forcing effect. This is often determined from long-term data, covering several decades, such as global solar radiation measurements [e.g., *Liepert and Kukla*, 1997]. Since our study was conducted only during a very limited period of time, it is not feasible to determine any meaningful radiative forcing informa-

tion from our data. Nevertheless, in this study, the effect of aerosol on solar radiation attenuation, on a very small (time) scale, may be illustrated by considering the relationship between global (G) and diffuse (D) solar radiation measurements on days with different aerosol regimes. *Liepert and Kukla* [1997] indicated that higher values of G/D ratio could mean less aerosol scattering or more absorption.

Figure 12 shows the diurnal radiation curves for the two days (21 February and 01 March 1997) with the highest concentrations of dust and pollutants, respectively. Typically, solar radiation measurements begin at zero before sunrise, attain peak values around midday, and descend back to zero at sunset. To have an idea of the present day maximum peak global radiation value obtainable in Sde Boker, under cloudless skies and at background aerosol levels, we looked at measurements acquired at 10-minute intervals over a period of 3 years (1995-1997), and found the maximum peak value to be of the order of 1100 Wm^{-2}; occurring mostly during the summer months in each of the 3 years. A comparison of radiation and other aerosol data between the two days represented in Figure 11 helps to illustrate the effect of aerosol concentration and composition on the extinction of solar radiation (records of visual cloud observation show about 50% cloud cover on each of those two days). On 21 February, there was a strong dust event with total aerosol volume exceeding 700 $\mu m^3/cm^3$, and aerosol scattering σ_{sp} attained almost 800 Mm^{-1} at the 550 nm wavelength (Figure 2A) and in fact at all three wavelengths. At the time of the measurement of the radiation data described by the curves in Figure 11A, the dust event which attained its maximum level in the early hours of that morning (Figure 2A) had subsided to some extent, although there was still ample aerosol in the atmosphere. Nevertheless, the measured global solar radiation was appreciably low (an average

of about 300 W/m^2), and equal to the diffuse radiation (Figure 11A). This produced a G/D ratio of 1 during a greater part of the day, showing that almost all the radiation was scattered. By contrast, on 1 March, there was only little dust with average aerosol volume less than 20 $\mu m^3/cm^3$ (see also Table 1), producing moderate scattering (σ_{sp} was about 100 Mm^{-1} at all three wavelengths) (Figure 2B), but the measured global radiation reached 800 W/m^2 with diffuse radiation averaging only about 180 W/m^2 (Figure 11B), resulting in fairly high G/D ratios. Since scattering was not particularly low, the high G/D value may be due to absorption by some of the pollutants.

6 CONCLUSIONS

The measurement and analysis of several parameters related to aerosol optical characteristics has provided a better understanding of the aerosol radiative effects at a remote site in the Eastern Mediterranean arid zone. The study period in late winter was characterized by the influence of a few intense dust events originating mostly on the Sinai Peninsula and nearby North Africa, and several pollution events with a prominent contribution from sources in Israel. These events present conditions markedly different from the situation in summer when the site is dominated by aerosols from long-range transport originating in Europe [*Gertler et al.*, 1994; *Luria et al.*, 1996]. During dust events, the coarse mode aerosol dominated light scattering, while outside of these episodes the fine mode accounted for most of the scattering. Dust- and pollution dominated periods could be clearly identified from aerosol parameters, such as the relative volume concentrations in the fine and coarse modes, from optical parameters such as the Ångstrom coefficient,

and from gaseous tracers, such as CO and SO_2. Short-lived gaseous and particulate tracers (e.g., SO_2 and CN) confirmed the importance of regional pollution sources during the study period. Mass and volume scattering efficiencies could be obtained by multivariate regression analysis, using coarse and fine fraction data as independent variables.

Plots of the aerosol size distribution from our campaign show that dust storms cause an increase in the number and volume of coarse sized particles (diameter>1 μm) but do not have a strong effect on the submicron part of the size spectra. An analysis of the chemical composition of the aerosol reveals that these large particles are composed mainly of calcium (Ca), silicon (Si) and associated elements, which are indicators of mineral dust. On the other hand, apart from dusty periods when these elements also are important in the fine fraction, this size range is generally dominated by sulfur (S), presumably present as sulfates. Fine sulfur and fine black carbon were correlated, suggesting that they originate from the same sources or source areas.

Comparison of scattering and radiation measurements on two different days under quite different aerosol regimes has shown, on a short time scale, the considerable attenuating effect of high aerosol loading on solar radiation.

ACKNOWLEDGEMENTS

This research was supported by the Max Planck Society, Germany, and by the Belgian Federal Office for Scientific, Technical and Cultural Affairs, the Special Research Fund of the University of Gent, and the "Fonds voor Wetenschappelijk Onderzoek - Vlaanderen". We thank the Solar Energy Research Center of the Jacob Blaustein Institute for Desert Research, Sde Boker, Israel, for providing us with their meteorological data, as well as the German Weather Service for making available the air-mass back trajectory data.

REFERENCES

Anderson, T. L., D. S. Covert, S. F. Marshal, M. L. Laucks, R. J. Charlson, A. P. Waggoner, J. A. Ogren, R. Caldow, R. L. Holm, F. R. Quant, G. J. Sem, A. Wiedensohler, N. A. Ahlquist, and T. S. Bates, Performance characteristics of a high-sensitivity, three-wavelength, total scatter/backscatter nephelometer. *Journal of Atmospheric and Oceanic Technology*, *13*, 967-986, 1996.

Andreae, M. O., Soot carbon and excess fine potassium: long-range transport of combustion derived aerosols. *Science*, *220*, 1148-1151, 1983.

Andreae, M. O., T. W. Andreae, R. J. Ferek, and H. Raemdonck, Long-range transport of soot carbon in the marine atmosphere. *Sci. Total Environ.*, *36*, 73-80, 1984

Birch, M.E. and R.A. Cary, Elemental carbon-based method for monitoring occupational exposures to particulate diesel exhaust, *Aerosol Sci. Technol.*, *25*(3), 221-241, 1996.

Bodhaine, B. A., Aerosol absorption measurements at Barrow, Mauna Loa and the South Pole. *Journal of Geophysical Research*, *100*, 8967-8975, 1995.

Bohren, C. F. and D. R. Huffman. *Absorption and Scattering of Light by Small Particles*. John Wiley & Sons, New York, 530 pp, 1983.

Charlson, R. J., S. E. Schwartz, J. M. Hales, R. D. Cess, J. A. Coakley, Jr., J. E. Hansen,

and D. J. Hofmann, Climate forcing by anthropogenic aerosols. *Science*, *255*, 423-430, 1992.

d'Almeida, G., On the variability of desert aerosol characteristics. *Journal of Geophysical Research*, *92*, 3017-3026, 1987.

Gertler, A. W., A preliminary apportionment of the sources of fine particulates impacting on the Israeli coast, *Israel Journal of Chemistry, 34*, 425-433, 1994.

Hänel, G., The properties of atmospheric aerosol particles as functions of the relative humidity at thermodynamic equilibrium with the surrounding moist air. *Advanced Geophysics*, *19*, 73-188, 1976.

Hansen, A.D.A., H. Rosen, and T. Novakov, The Aethalometer – an instrument for the real-time measurement of optical absorption by aerosol particles. *The Science of the Total Environment*, *36*, 191-196, 1984.

Hegg, D. A., D. S. Covert, M. J. Rood, P. V. Hobbs, Measurements of aerosol optical properties in marine air. *Journal of Geophysical Research*, *101*, 12,893-12,903, 1996a.

Hegg, D. A., P. V. Hobbs, S. Gasso, J. D. Nance, A. l. Rangno, Aerosol measurements in the Arctic relevant to direct and indirect radiative forcing. *Journal of Geophysical Research*, *101*, 23,349-23,363, 1996b.

Hegg, D. A., J. Livingston, P. V. Hobbs, T. Novakov, and P. Russell, Chemical apportionment of aerosol column optical depth off the mid-Atlantic coast of the United States. *Journal of Geophysical Research, 102*, 25,293-25,303, 1997.

Heintzenberg, J. and R.J. Charlson, Design and applications of the integrating nephelometer: A review. *Journal of Atmospheric and Oceanic Technology, 13*, 987-1000, 1996.

Heintzenberg, J. and H. Quenzel, On the effect of the loss of large particles on the determination of scattering coefficients with integrating nephelometers. *Atmospheric Environment, 7*, 503-507, 1973.

Horvath, H., Atmospheric light absorption - A review. *Atmospheric Environment, 27A*, 293-317, 1993.

IPCC (Intergovernmental Panel on Climate Change), *Climate Change: The IPCC Scientific Assessment*, edited by J. T. Houghton, G. J. Jenkins, and J. J. Ephraums, Report prepared for IPCC by Working Group 1, Cambridge University Press, 1990.

Kiehl, J. T. and B. P. Briegleb, The relative roles of sulfate aerosols and greenhouse gases in climate forcing. *Science, 260*, 311-314, 1993.

Liepert, B. G. and G. J. Kukla, Decline in global solar radiation with increased horizontal visibility in Germany between 1964 and 1900. *Journal of Climate*, *10*, 2391-2401, 1997.

Luria, M., M. Peleg, G. Sharf, D. S. Tov-Alper, N. Spitz, Y. Ben Ami, Z. Gawii, B. Lifschitz, A. Yitzchaki, and I. Seter, Atmospheric sulfur over the east Mediterranean region, J. Geophys. Res., *101*, 25,917-25,930, 1996.

Maenhaut, W., Composition and origin of the regional atmospheric aerosol at great distance from anthropogenic source areas. Assessment of the extent of the anthropogenic perturbation, Belgian Impulse Programme "Global Change" 1990-1996, Final Report, Federal Office for Scientific, Technical and Cultural Affairs, 105 pp, 1997.

Maenhaut, W., F. François, and J. Cafmeyer, The "Gent" stacked filter unit (SFU) sampler for the collection of aerosols in two size fractions: Description and instructions for installation and use. In*: Applied Research on Air Pollution using Nuclear-Related Analytical Techniques*, NAHRES-19, IAEA, Vienna, pp. 249-263, 1994.

Maenhaut, W., R. Hillamo, T. Mäkelä, J.L. Jaffrezo, M.H. Bergin, and C.I. Davidson, A new cascade impactor for aerosol sampling with subsequent PIXE analysis. *Nuclear Instruments and Methods in Physics Research, B109/110*, 482-487, 1996a.

Maenhaut, W, R. Salomonovic, J. Cafmeyer, C. Ichoku, A. Karnieli, and M. O. Andreae, Anthropogenic and natural radiatively active aerosol types at Sede Boker, Israel. *Journal of Aerosol Science*, *27*(1), S47-S48, 1996b.

Maenhaut, W., J. Cafmeyer, J. Ptasisnki, M. O. Andreae, T. W. Andreae, W. Elbert, F. X. Meixner, A. Karnieli, and, C. Ichoku, Chemical composition and light scattering of the atmospheric aerosol at a remote site in the Negev desert, Israel. *Journal of Aerosol Science*, *28*(1), S73-S74, 1997.

Mason B. and C. B. Moore, *Principles of Geochemistry* (Fourth Edition), John Wiley & Sons, New York, 344 pp, 1982.

Mie, G., Beitrage zur Optik trüber Medien, speziell kolloidaler Metallösungen, *Ann. Phys.*, *25*, 377-445, 1908.

Moulin, C., F. Dulac, C. E. Lambert, P. Chazette, B. Chatenet, and F. Lavenu, Long-term daily monitoring of Saharan dust load over ocean using Meteosat ISCCP-B2 data - 2. Accuracy of the method and validation using Sun photometer measurements. *Journal of Geophysical Research*, *102*, 16,959-16,969, 1997a.

Moulin, C., F. Guillard, F. Dulac, and C. E. Lambert, Long-term daily monitoring of Saharan dust load over ocean using Meteosat ISCCP-B2 data - 1. Methodology and preliminary results for 1983-1994 in the Mediterranean. *Journal of Geophysical Research*,

102, 16,947-16,958, 1997b.

Nagel, D., A. Herber, L. W. Thomason, and U. Leiterer, Vertical distribution of the spectral aerosol optical depth in the Arctic from 1993 to 1996. *Journal of Geophysical Research*, *103*, 1857-1870, 1998.

Nakajima, T., M. Tanaka, and T. Yamauchi, Retrieval of the optical properties of aerosols from aureole and extinction data. *Applied Optics*, *22*, 2951-2959, 1983.

Patterson, E.M., Optical properties of the crustal aerosols: relation to chemical and physical characteristics. *Journal of Geophysical Research*, *86*, 3236-3246, 1981.

Patterson, E.M., D. A. Gillette, and B. H. Stockton, Complex index of refraction between 300 and 700 nm for Saharan aerosols. *Journal of Geophysical Research*, *82*, 3153-3160, 1977.

Petzold, A., C. Kopp, and R. Niessner, The dependence of the specific attenuation cross-section on black carbon mass fraction and particle size. *Atmospheric Environment*, *31*, 661-672, 1997.

Remer, L. A., S. Gassó, D. A. Hegg, Y. J. Kaufman, and B. N. Holben, Urban/industrial aerosol: Ground-based Sun/sky radiometer and airborne in situ measurements. *Journal of Geophysical Research*, *102*, 16,849-16,859, 1997.

Sagan, C. and J. B. Pollack, Anisotropic nonconservative scattering and the clouds of Venus. *Journal of Geophysical Research, 72*, 469-477, 1967.

Schwartz, S. E. and M. O. Andreae, Uncertainty in climate change caused by aerosols. *Science, 272*, 1121-1122, 1996.

Seinfeld, J. H., *Air Pollution – Physical and Chemical Fundamentals*, McGraw-Hill Book Company, New York, 523 pp, 1975.

Seinfeld, J. H. and S. N. Pandis, *Atmospheric Chemistry and Physics: From Air Pollution to Climate Change*. John Wiley, New York, 1360 pp., 1997.

Taylor, K. E., and J. E. Penner, Response of the climate system to atmospheric aerosols and greenhouse gases. *Nature, 369*, 734-737, 1994.

Tegen, I, and A. A. Lacis, Modeling of particle size distribution and its influence on the radiative properties of mineral dust aerosol, *Journal of Geophysical Research, 101*, 19,237-19,244, 1996.

Tegen, I, A. A. Lacis, and I Fung, The influence on climate forcing of mineral aerosols from disturbed soils. *Nature, 380*, 419-422, 1996.

Twomey, S, Aerosols, clouds and radiation, *Atmospheric Environment*, Part A-General Topics, 25, 2435-2442, 1991.

Wendisch, M. and W. von Hoyningen-Huene, Possibility of refractive index determination of atmospheric aerosol particles by ground-based solar extinction and scattering measurements. *Atmospheric Environment*, *28*, 785-792, 1994.

Wiscombe, W. J. and G. W. Grams, The backscattered fraction in two-stream approximations. *Journal of the Atmospheric Sciences*, *33*, 2440-2451, 1976.

FIGURE CAPTIONS

Figure 1: Time series plots (Universal Times in 1997) produced from 10-minute averages of:

A. Aerosol scattering coefficients σ_{sp} at 550 nm wavelength.

B. Ångstrom exponents α at 550 nm wavelength (computed from the nephelometer σ_{sp} measurements).

C. Coarse (1.0 to 3.3 μm) aerosol particle number concentrations (number of particles per cm^3).

D. Fine (0.11 to 1.0 μm) particle number concentrations (number of particles per cm^3).

E. Coarse (1.0 to 3.3 μm) aerosol volume concentration ([μm^3] of particles per cm^3).

F. Fine (0.11 to 1.0 μm) aerosol volume concentration ([μm^3] of particles per cm^3).

G. Aerosol backscattered fractions (σ_{bsp}/σ_{sp} ratio) at 550 nm wavelength (computed from the nephelometer σ_{sp} and σ_{bsp} measurements).

H. Black Carbon Equivalent (BCE) concentrations (ng/m^3).

I. Aerosol single-scattering albedo ω at 550 nm wavelength (computed from the nephelometer σ_{sp} and aethalometer σ_{ap} measurements).

J. Carbon monoxide CO concentrations.

K. Carbon dioxide CO_2 concentrations.

L. Sulfur dioxide SO_2 concentrations.

M. Aitken Condensation Nuclei CN concentrations.

Figure 2: Comparison of aerosol scattering coefficients measured by the nephelometer with those simulated from the PMS-PCASP number concentration measurements based

on different refractive indices (whose real and imaginary parts are preceded by 'r' and 'i' in the legend) for two segments of the campaign period with different aerosol regimes (note the difference in vertical axis scale):

(a) highest dust (21 February 1997).

(b) highest pollution (1 March 1997).

Figure 3: Aerosol number size distribution for 5 days with different aerosol regimes (see characteristics in Table 1). The date of each chart is indicated, and the Universal Times of the individual plots are shown in the legends.

Figure 4: Aerosol volume size distribution plots for 5 days with different aerosol regimes (see characteristics in Table 1). The date of each chart is indicated, and the Universal Times of the individual plots are shown in the legends.

Figure 5: Aerosol particulate mass measurements from the SNN and SNT mass samplers in the:

(a) Coarse size range (2-10 μm equivalent aerodynamic diameter (EAD)).

(b) Fine size range (<2 μm EAD).

Figure 6: Comparison of the trends of aerosol particle mass (coarse and fine from the SFU-SNN) and scattering coefficients (from the nephelometer).

Figure 7: Aerosol mass concentrations of selected elements (from the SFU-SNN mass

samplers) in the:

(a) Coarse size range (2-10 μm equivalent aerodynamic diameter (EAD)).

(b) Fine size range (<2 μm EAD).

Figure 8: Comparison of black carbon concentrations measured by the aethalometer with corresponding coarse and fine measurements from the SFU-SNN.

Figure 9: Aerosol main constituents determined from the SFU-SNN measurements, based on the concentrations of chemical trace elements in the Earth's crust and sea water as given in *Mason and Moore* [1982]. Note that the columns labeled 20-Feb-97 represent the data for the nighttime period, which covers the early morning of the 21st corresponding to the target period in Table 1:

(a) Fine size fractions

(b) Coarse size fractions

Figure 10: Mass size distributions of the selected elements from the SDI for the 5 selected periods of different aerosol regimes (see characteristics in Table 1).

Figure 11: Global and diffuse radiation measurements from routine meteorological observations for two dates with the widest difference in aerosol composition during the campaign:

(a) Highest dust (21 February 1997).

(b) Highest pollution (01 March 1997).

FIG 1

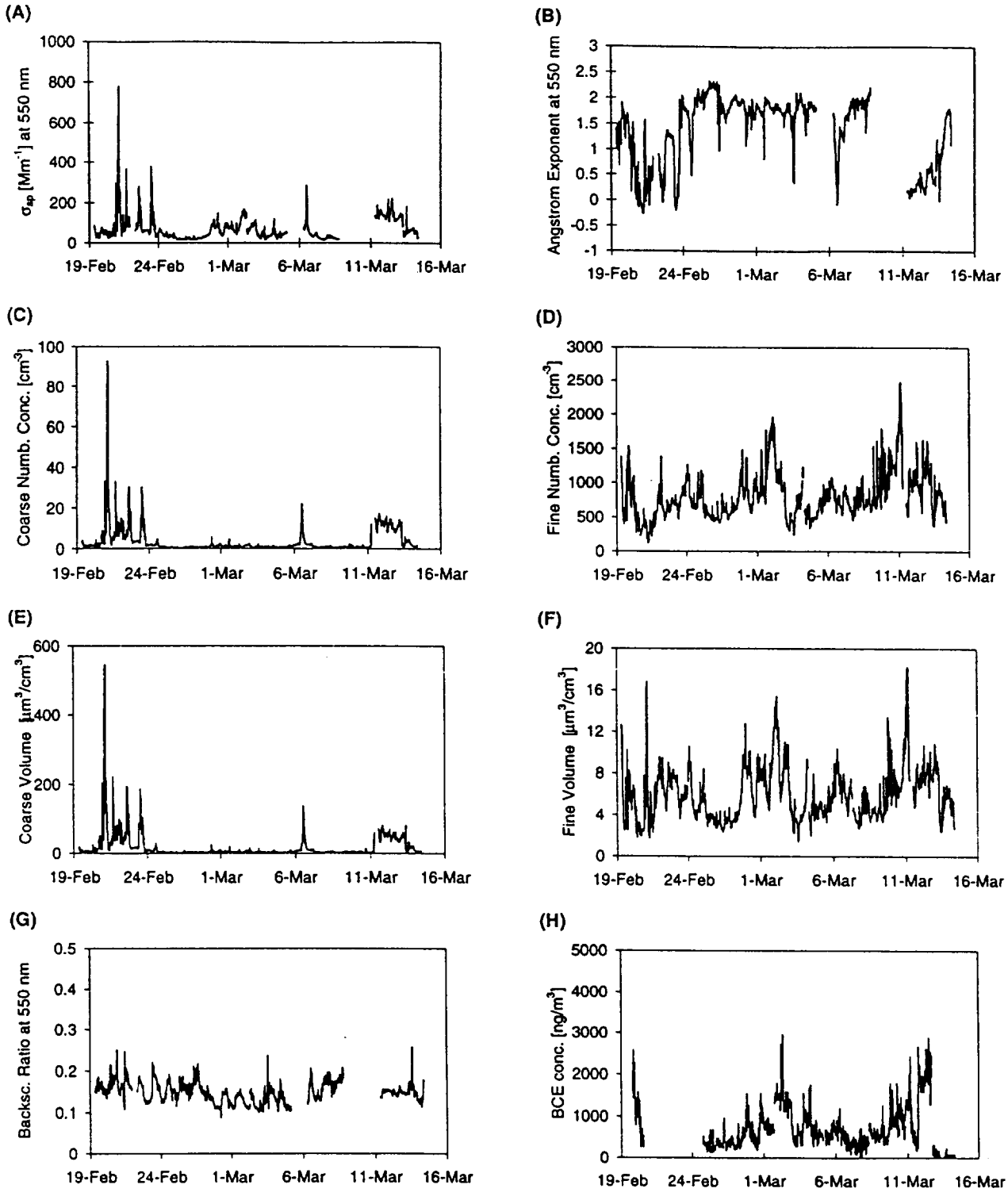
(A)
σ_{sp} [Mm^{-1}] at 550 nm
1000
800
600
400
200
0
19-Feb
24-Feb
1-Mar
6-Mar
11-Mar
16-Mar
(B)
Angstrom Exponent at 550 nm
3
2.5
2
1.5
1
0.5
0
-0.5
-1
19-Feb
24-Feb
1-Mar
6-Mar
11-Mar
15-Mar
(C)
Coarse Numb. Conc. [cm^{-3}]
100
80
60
40
20
0
19-Feb
24-Feb
1-Mar
6-Mar
11-Mar
16-Mar
(D)
Fine Numb. Conc. [cm^{-3}]
3000
2500
2000
1500
1000
500
0
19-Feb
24-Feb
1-Mar
6-Mar
11-Mar
16-Mar
(E)
Coarse Volume [µm^3/cm^3]
600
400
200
0
19-Feb
24-Feb
1-Mar
6-Mar
11-Mar
16-Mar
(F)
Fine Volume [µm^3/cm^3]
20
16
12
8
4
0
19-Feb
24-Feb
1-Mar
6-Mar
11-Mar
16-Mar
(G)
Backsc. Ratio at 550 nm
0.5
0.4
0.3
0.2
0.1
0
19-Feb
24-Feb
1-Mar
6-Mar
11-Mar
16-Mar
(H)
BCE conc. [ng/m^3]
5000
4000
3000
2000
1000
0
19-Feb
24-Feb
1-Mar
6-Mar
11-Mar
16-Mar

FIG 1 CONTD

(I)

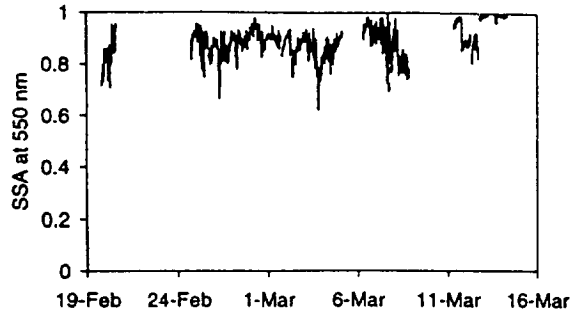

(J)

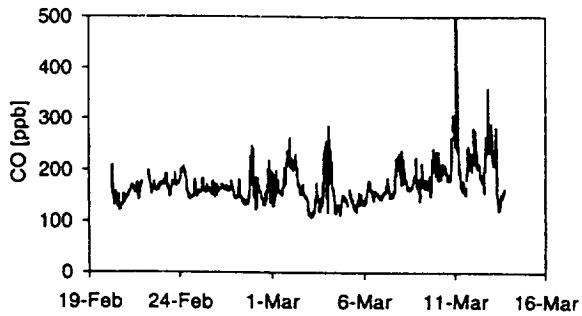

(K)

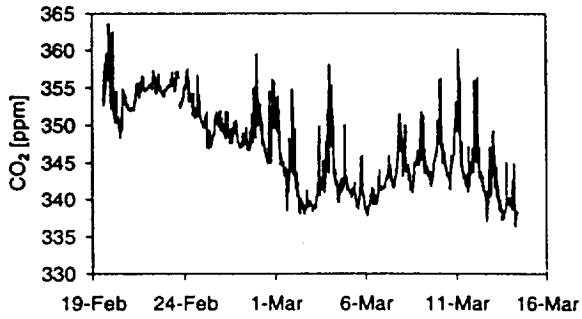

(L)

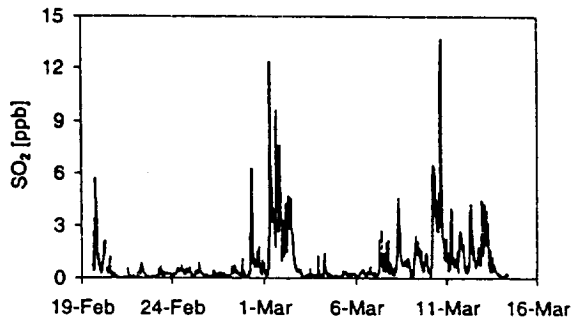

(M)

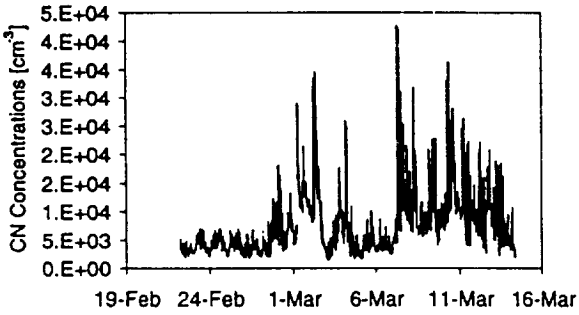

FIG. 2

(A)

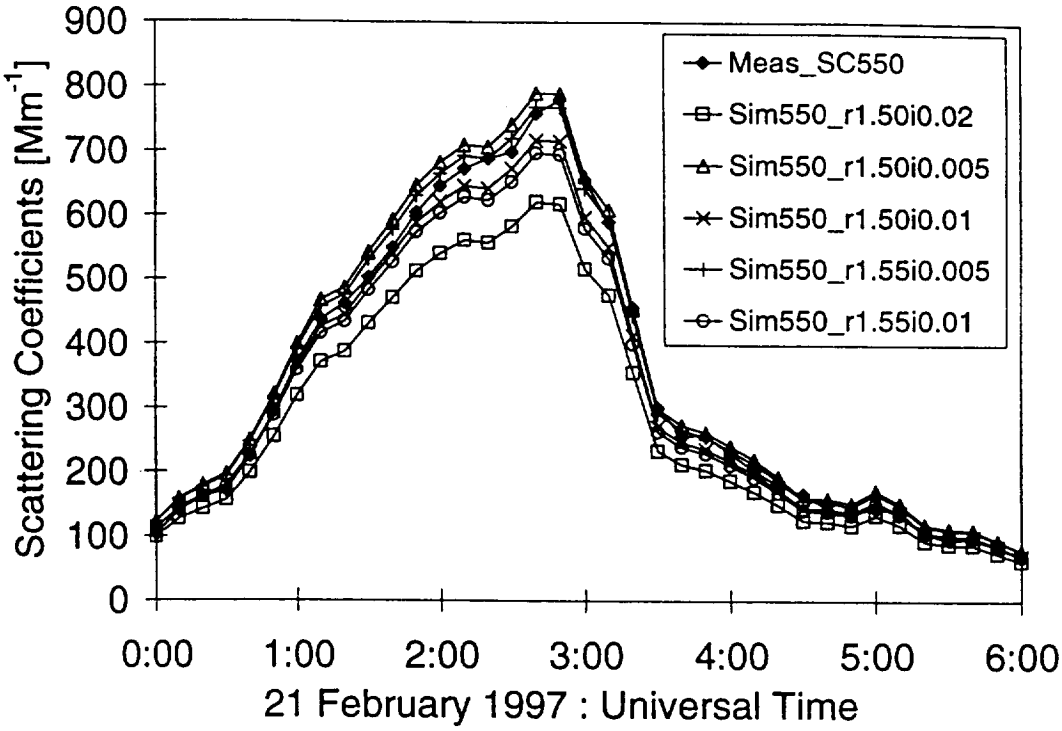
Scattering Coefficients [Mm-1]
900
800
700
600
500
400
300
200
100
0
0:00
1:00
2:00
3:00
4:00
5:00
6:00
21 February 1997 : Universal Time
Meas_SC550
Sim550_r1.50i0.02
Sim550_r1.50i0.005
Sim550_r1.50i0.01
Sim550_r1.55i0.005
Sim550_r1.55i0.01

(B)

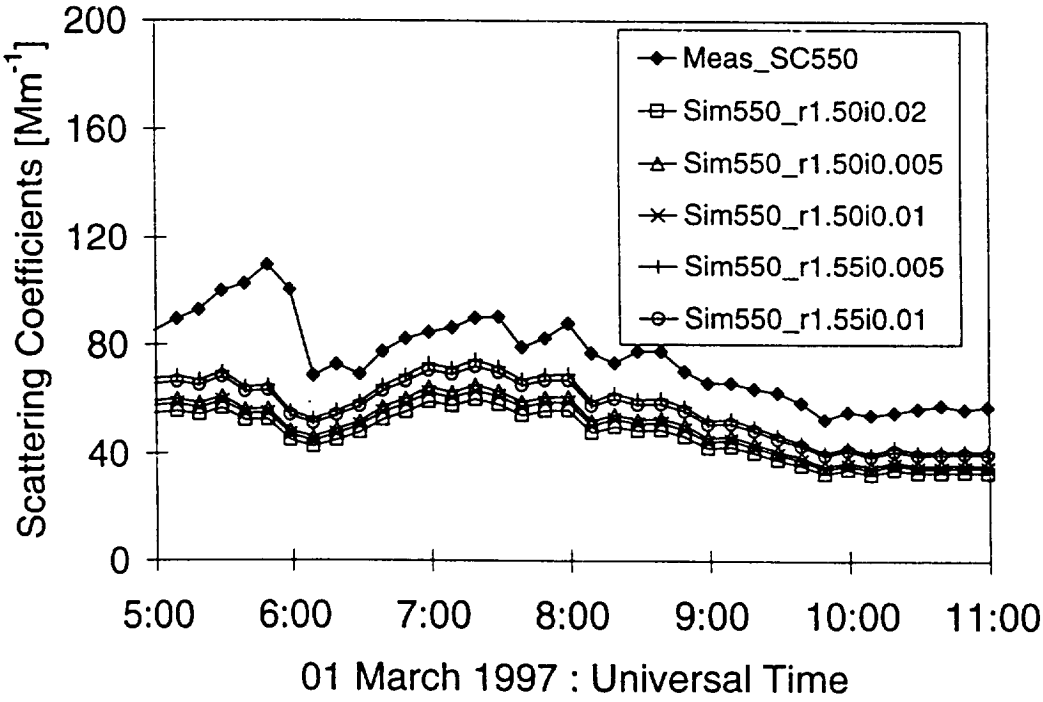
Scattering Coefficients [Mm-1]
200
160
120
80
40
0
5:00
6:00
7:00
8:00
9:00
10:00
11:00
01 March 1997 : Universal Time
Meas_SC550
Sim550_r1.50i0.02
Sim550_r1.50i0.005
Sim550_r1.50i0.01
Sim550_r1.55i0.005
Sim550_r1.55i0.01

FIG. 3

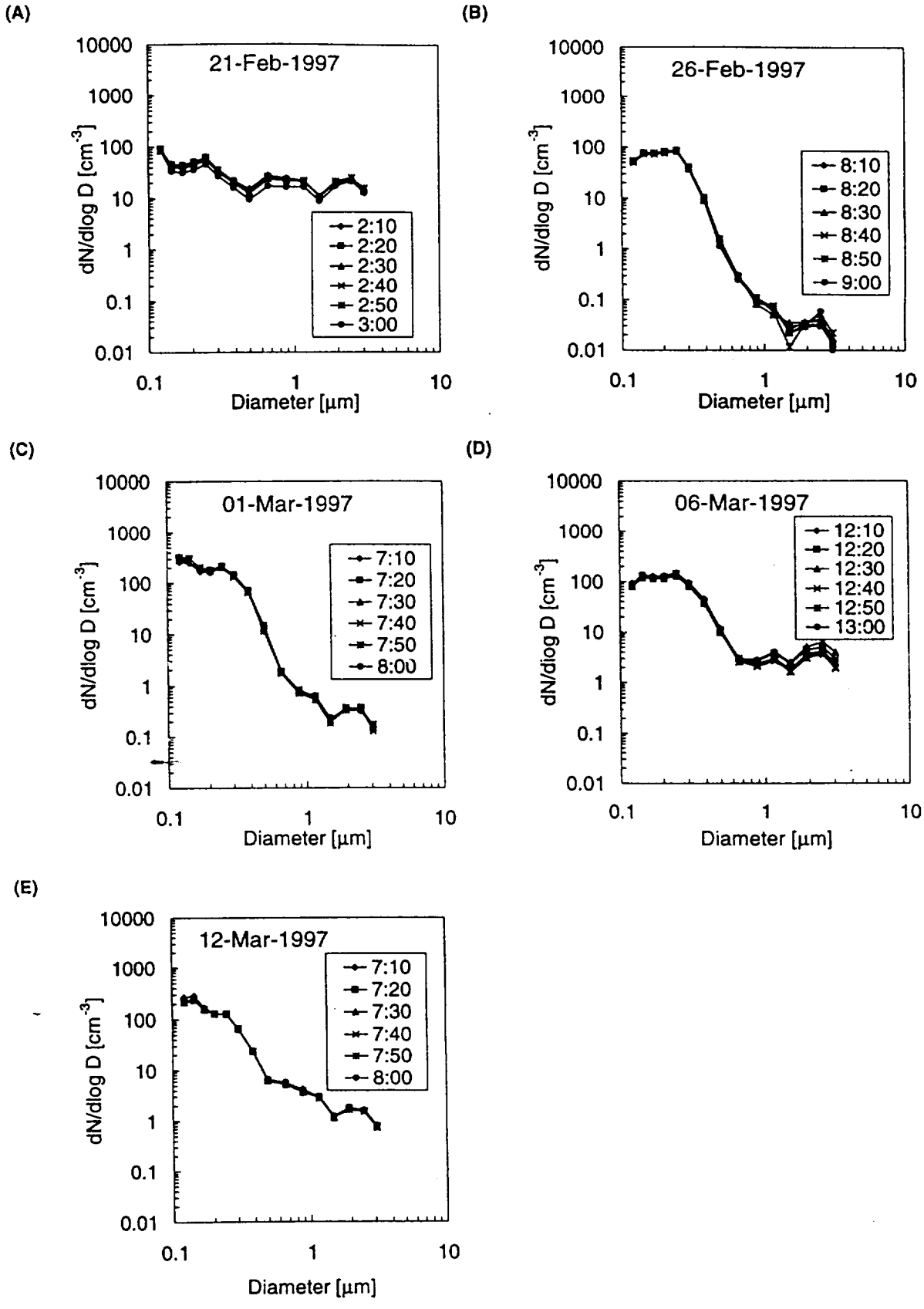
(A)
21-Feb-1997
2:10
2:20
2:30
2:40
2:50
3:00
(B)
26-Feb-1997
8:10
8:20
8:30
8:40
8:50
9:00
(C)
01-Mar-1997
7:10
7:20
7:30
7:40
7:50
8:00
(D)
06-Mar-1997
12:10
12:20
12:30
12:40
12:50
13:00
(E)
12-Mar-1997
7:10
7:20
7:30
7:40
7:50
8:00
dN/dlog D [cm-3]
Diameter [µm]
10000
1000
100
10
1
0.1
0.01
0.1
1
10

FIG. 4

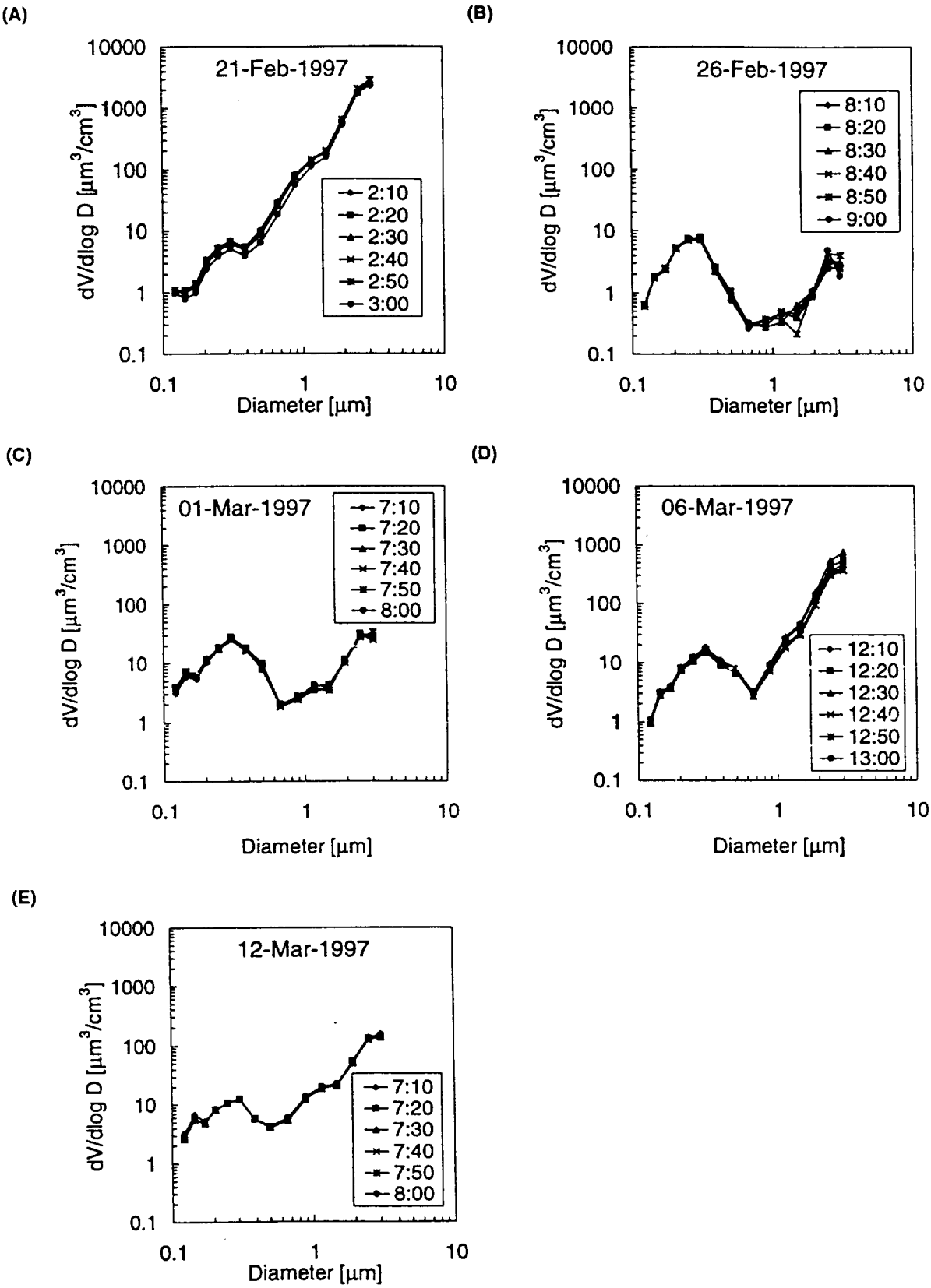
(A)
21-Feb-1997
2:10
2:20
2:30
2:40
2:50
3:00
(B)
26-Feb-1997
8:10
8:20
8:30
8:40
8:50
9:00
(C)
01-Mar-1997
7:10
7:20
7:30
7:40
7:50
8:00
(D)
06-Mar-1997
12:10
12:20
12:30
12:40
12:50
13:00
(E)
12-Mar-1997
7:10
7:20
7:30
7:40
7:50
8:00
dV/dlog D [µm³/cm³]
Diameter [µm]
10000
1000
100
10
1
0.1
0.1
1
10

FIG. 5

(A)

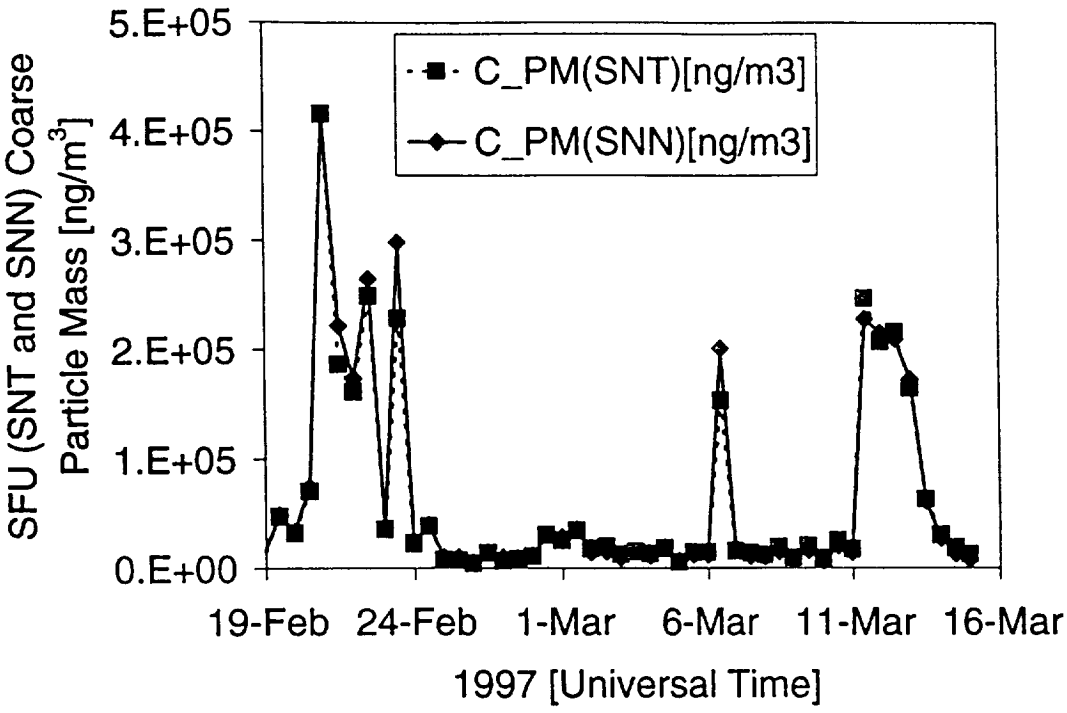
5.E+05
4.E+05
3.E+05
2.E+05
1.E+05
0.E+00
SFU (SNT and SNN) Coarse Particle Mass [ng/m3]
C_PM(SNT)[ng/m3]
C_PM(SNN)[ng/m3]
19-Feb
24-Feb
1-Mar
6-Mar
11-Mar
16-Mar
1997 [Universal Time]

(B)

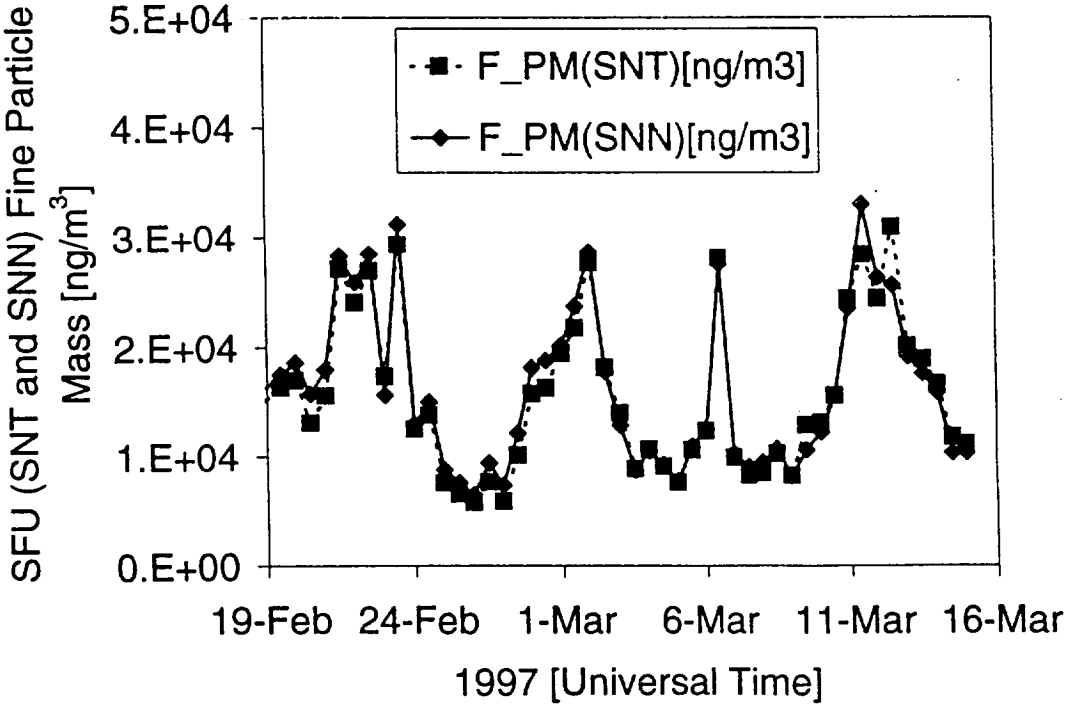
5.E+04
4.E+04
3.E+04
2.E+04
1.E+04
0.E+00
SFU (SNT and SNN) Fine Particle Mass [ng/m3]
F_PM(SNT)[ng/m3]
F_PM(SNN)[ng/m3]
19-Feb
24-Feb
1-Mar
6-Mar
11-Mar
16-Mar
1997 [Universal Time]

FIG. 6

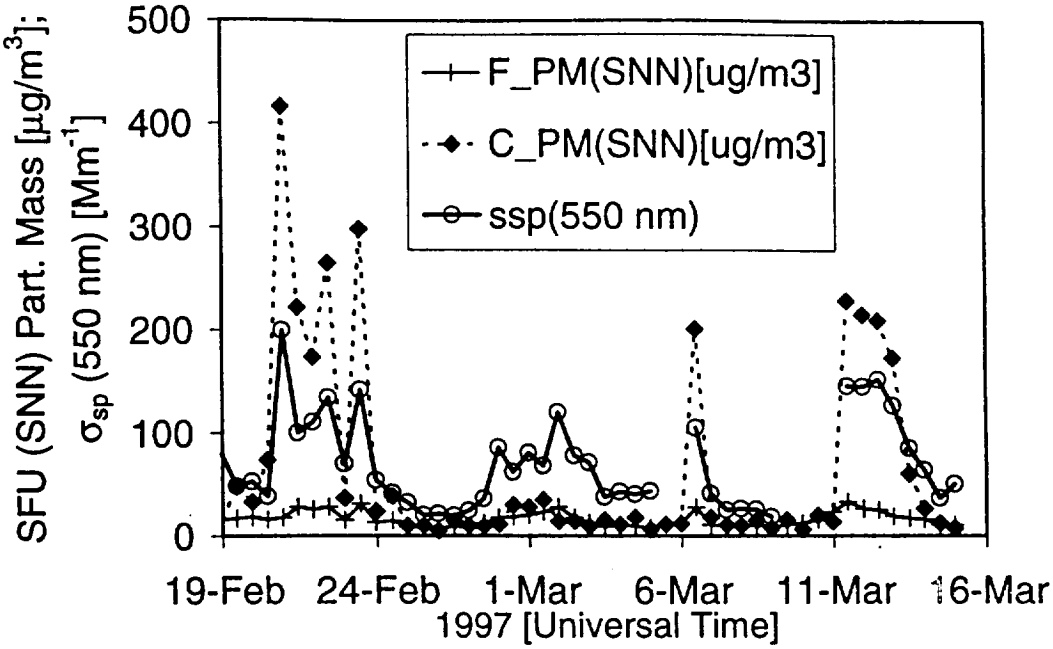
SFU (SNN) Part. Mass [µg/m3];
σsp (550 nm) [Mm-1]
500
400
300
200
100
0
F_PM(SNN)[ug/m3]
C_PM(SNN)[ug/m3]
ssp(550 nm)
19-Feb
24-Feb
1-Mar
6-Mar
11-Mar
16-Mar
1997 [Universal Time]

FIG. 7

(A)

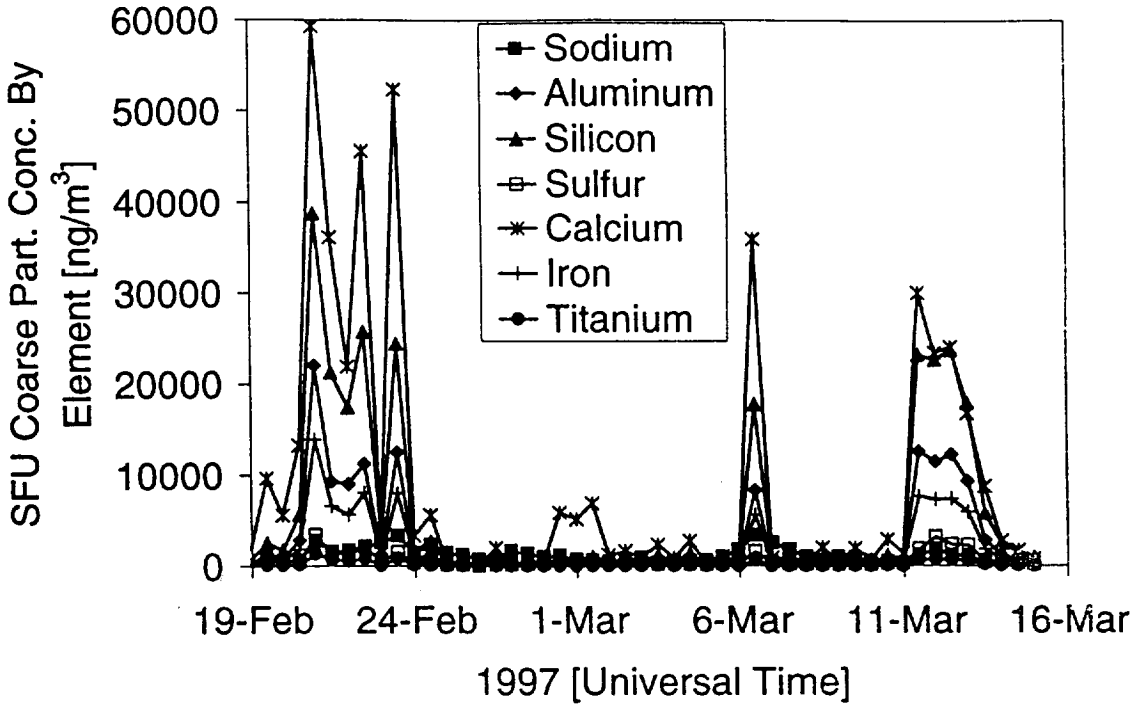
SFU Coarse Part. Conc. By Element [ng/m3]
60000
50000
40000
30000
20000
10000
0
Sodium
Aluminum
Silicon
Sulfur
Calcium
Iron
Titanium
19-Feb
24-Feb
1-Mar
6-Mar
11-Mar
16-Mar
1997 [Universal Time]

(B)

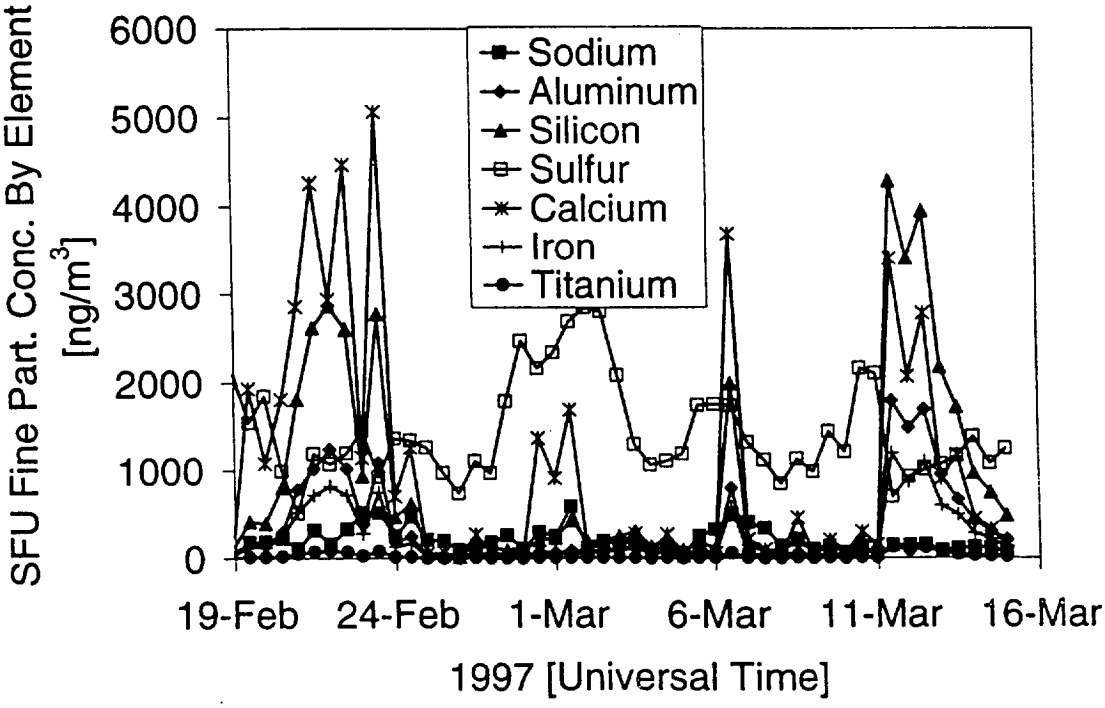
SFU Fine Part. Conc. By Element [ng/m3]
6000
5000
4000
3000
2000
1000
0
Sodium
Aluminum
Silicon
Sulfur
Calcium
Iron
Titanium
19-Feb
24-Feb
1-Mar
6-Mar
11-Mar
16-Mar
1997 [Universal Time]

FIG 8

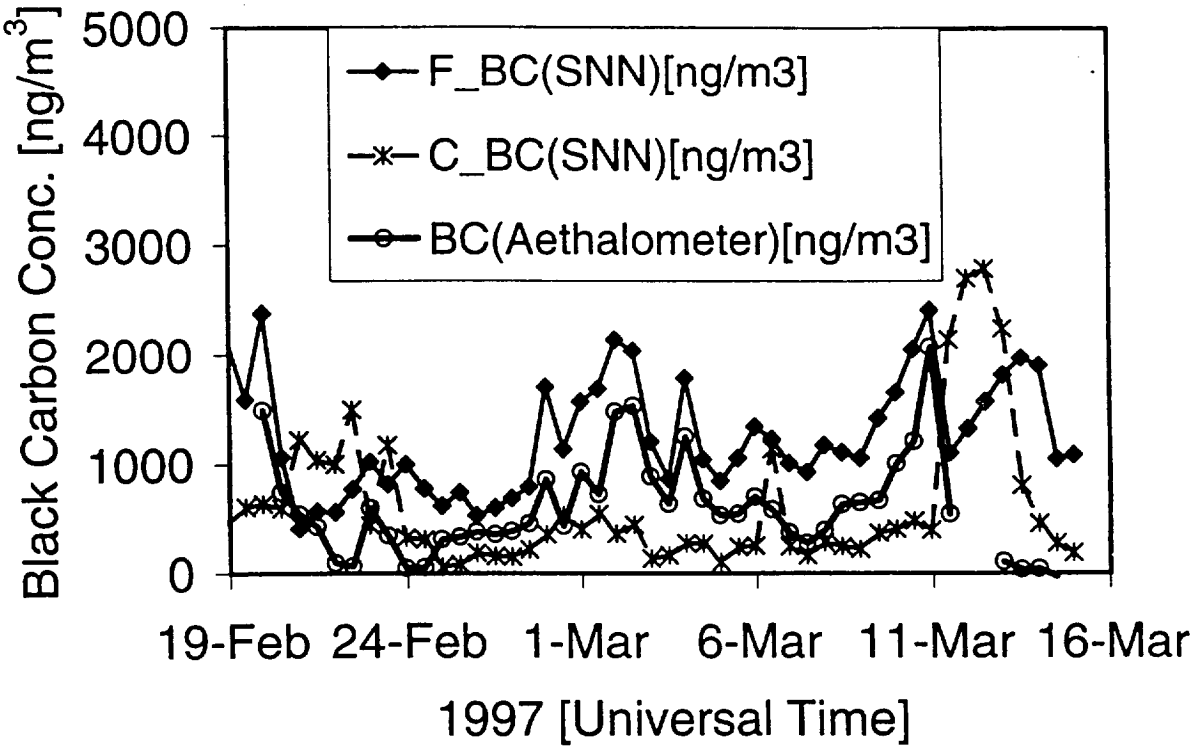
Black Carbon Conc. [ng/m3]
5000
4000
3000
2000
1000
0
F_BC(SNN)[ng/m3]
C_BC(SNN)[ng/m3]
BC(Aethalometer)[ng/m3]
19-Feb
24-Feb
1-Mar
6-Mar
11-Mar
16-Mar
1997 [Universal Time]

FIG 9

(A)

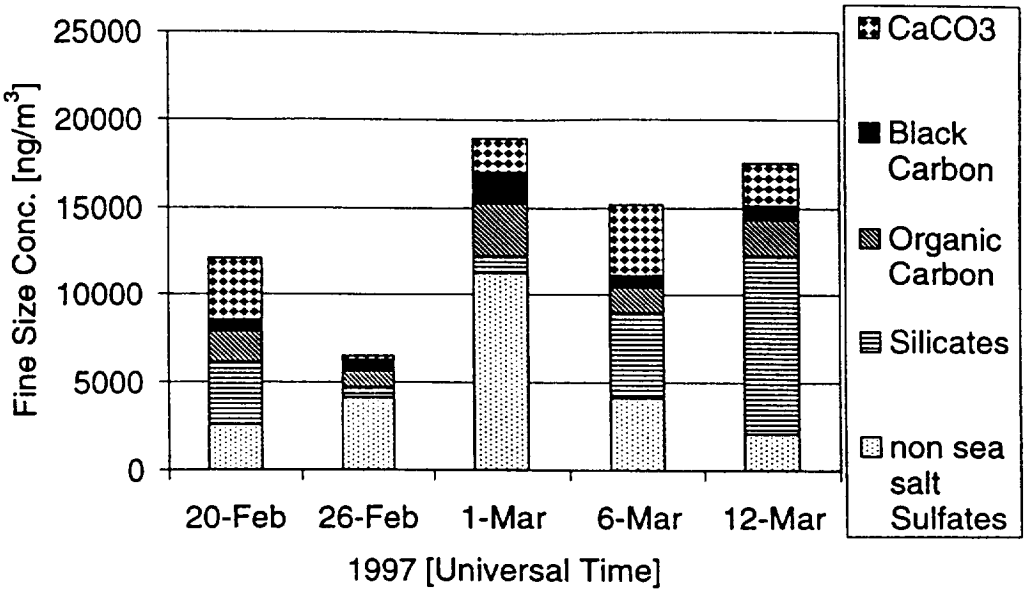
25000
20000
15000
10000
5000
0
Fine Size Conc. [ng/m3]
20-Feb
26-Feb
1-Mar
6-Mar
12-Mar
1997 [Universal Time]
CaCO3
Black Carbon
Organic Carbon
Silicates
non sea salt Sulfates

(B)

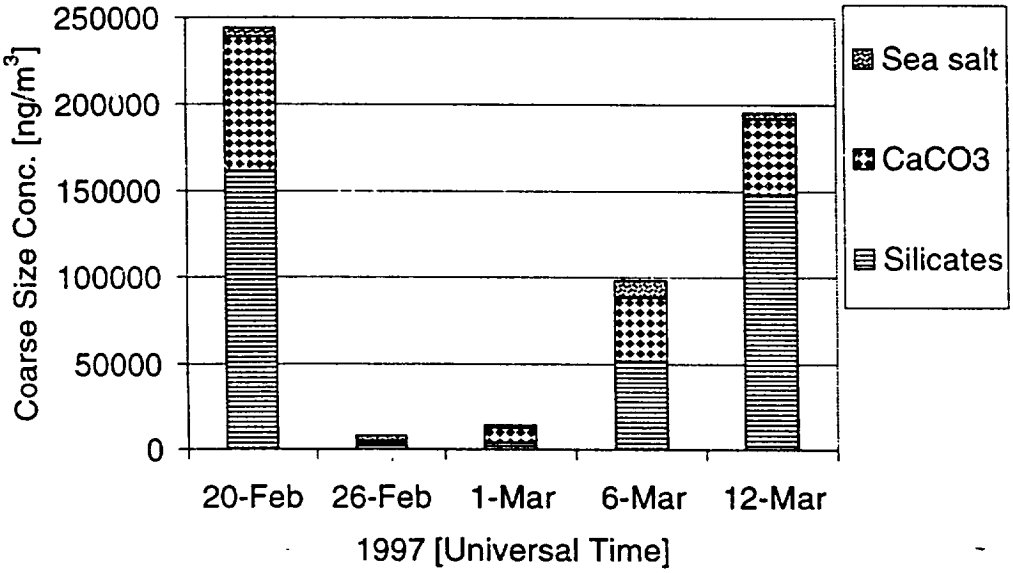
250000
200000
150000
100000
50000
0
Coarse Size Conc. [ng/m3]
20-Feb
26-Feb
1-Mar
6-Mar
12-Mar
1997 [Universal Time]
Sea salt
CaCO3
Silicates

FIG 10

(A)

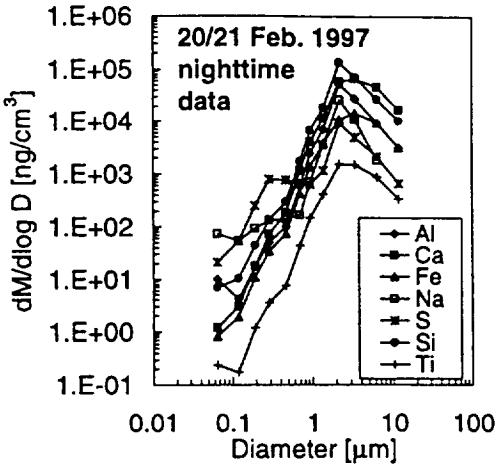
20/21 Feb. 1997
nighttime
data
dM/dlog D [ng/cm3]
1.E+06
1.E+05
1.E+04
1.E+03
1.E+02
1.E+01
1.E+00
1.E-01
0.01
0.1
1
10
100
Diameter [µm]
Al
Ca
Fe
Na
S
Si
Ti

(B)

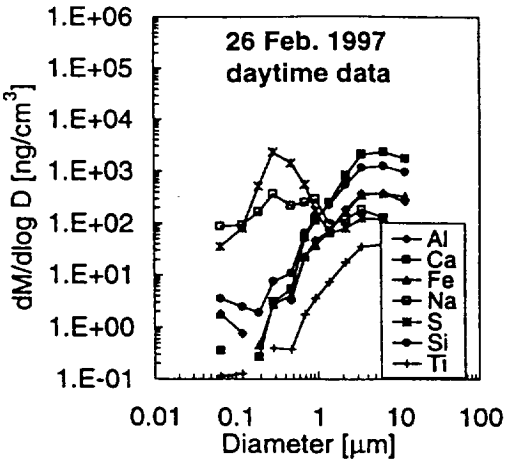
26 Feb. 1997
daytime data
dM/dlog D [ng/cm3]
1.E+06
1.E+05
1.E+04
1.E+03
1.E+02
1.E+01
1.E+00
1.E-01
0.01
0.1
1
10
100
Diameter [µm]
Al
Ca
Fe
Na
S
Si
Ti

(C)

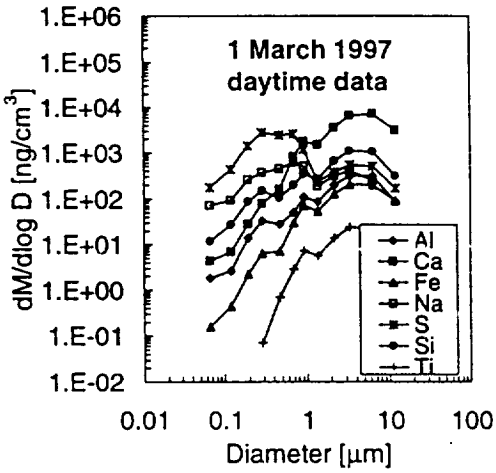
1 March 1997
daytime data
dM/dlog D [ng/cm3]
1.E+06
1.E+05
1.E+04
1.E+03
1.E+02
1.E+01
1.E+00
1.E-01
1.E-02
0.01
0.1
1
10
100
Diameter [µm]
Al
Ca
Fe
Na
S
Si
Ti

(D)

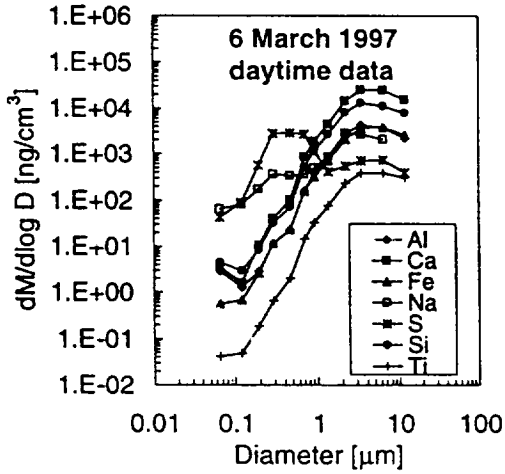
6 March 1997
daytime data
dM/dlog D [ng/cm3]
1.E+06
1.E+05
1.E+04
1.E+03
1.E+02
1.E+01
1.E+00
1.E-01
1.E-02
0.01
0.1
1
10
100
Diameter [µm]
Al
Ca
Fe
Na
S
Si
Ti

(E)

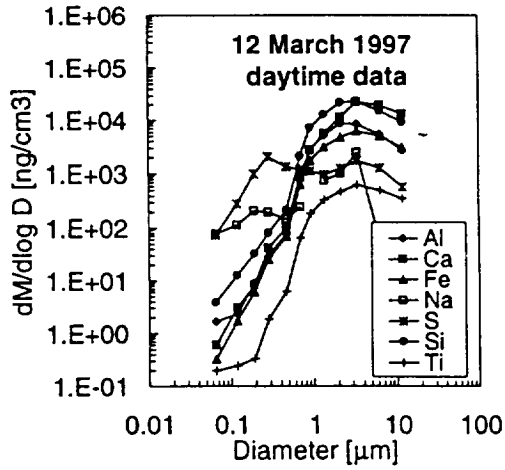
12 March 1997
daytime data
dM/dlog D [ng/cm3]
1.E+06
1.E+05
1.E+04
1.E+03
1.E+02
1.E+01
1.E+00
1.E-01
0.01
0.1
1
10
100
Diameter [µm]
Al
Ca
Fe
Na
S
Si
Ti

FIG 11

(A)

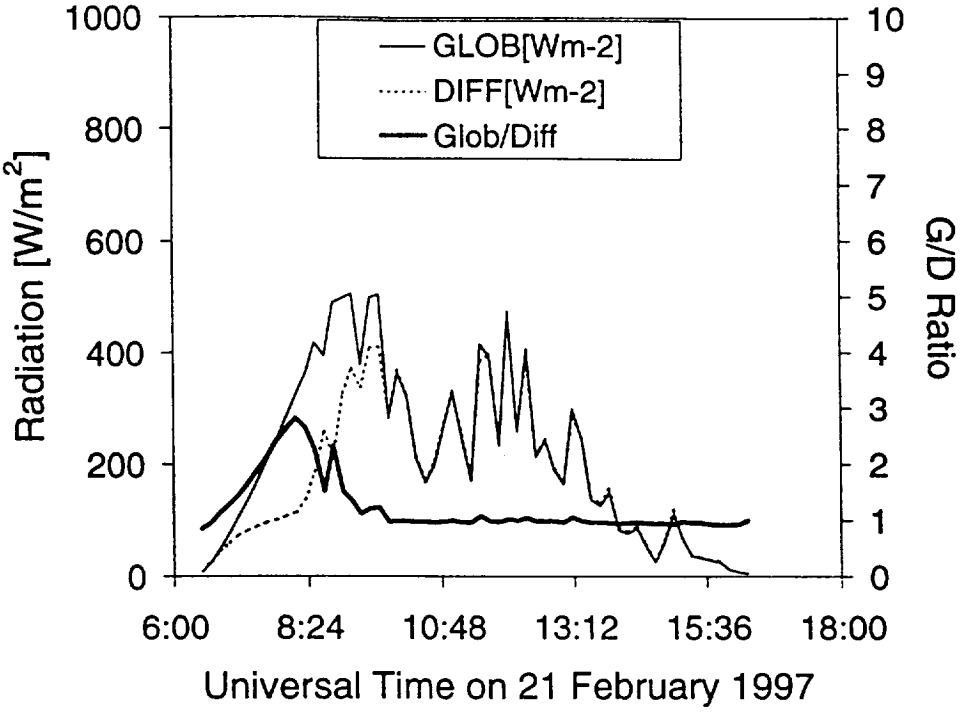
GLOB[Wm-2]
DIFF[Wm-2]
Glob/Diff
Radiation [W/m2]
G/D Ratio
1000
800
600
400
200
0
10
9
8
7
6
5
4
3
2
1
0
6:00
8:24
10:48
13:12
15:36
18:00
Universal Time on 21 February 1997

(B)

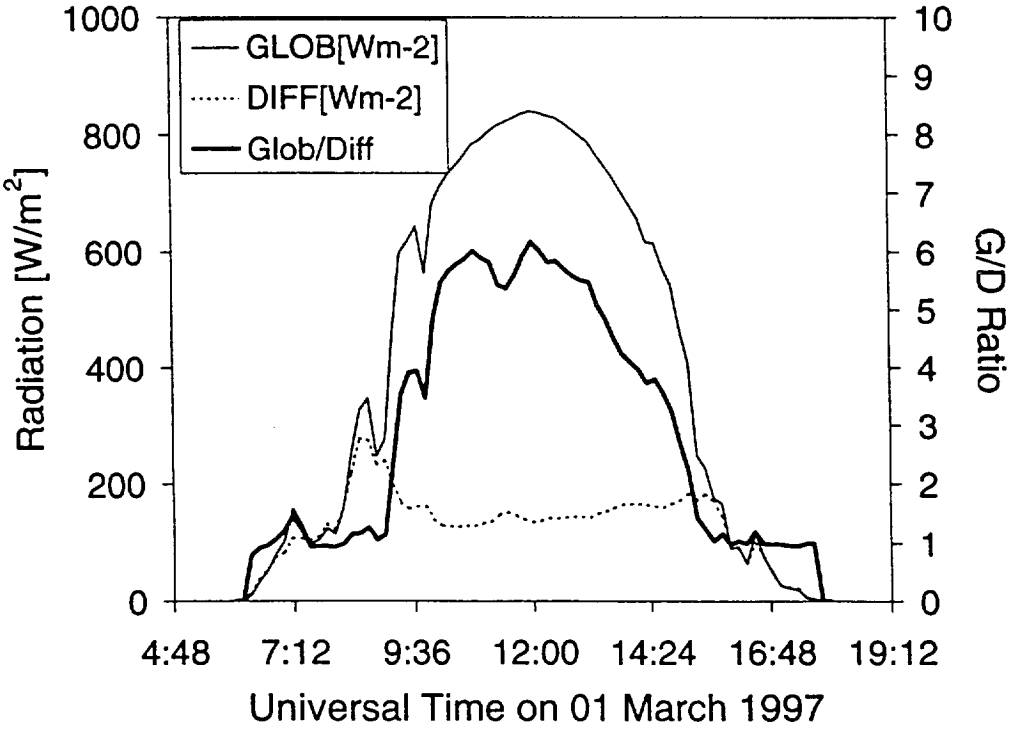
GLOB[Wm-2]
DIFF[Wm-2]
Glob/Diff
Radiation [W/m2]
G/D Ratio
1000
800
600
400
200
0
10
9
8
7
6
5
4
3
2
1
0
4:48
7:12
9:36
12:00
14:24
16:48
19:12
Universal Time on 01 March 1997

Table 1

Characteristics of target periods marking different aerosol regimes

Date	Start Time [UT]	End Time [UT]	Vol.[$\mu m^3/cm^3$]	BC[ng/m^3]	SO2[ppb]	CO[ppb]	CN[$1/cm^3$]	Dust Level	Pollution Level
21-Feb-97	2:00	3:00	510.6	431.4	0.007	149.7	N/A	High	Low
26-Feb-97	8:00	9:00	4.9	463.3	0.355	159.9	4670	Low	Low
1-Mar-97	7:00	8:00	16.8	861.4	9.610	177.9	22189	Low	Medium
6-Mar-97	12:00	13:00	101.7	571.1	0.113	149.2	3696	Medium	Low
12-Mar-97	7:00	8:00	42.2	N/A	3.857	206.8	7266	Medium	Medium

N/A denotes 'not available'

Table 2

Overall Correlation Coefficients (r) and root mean square errors (rmse) between Nephelometer-measured σ_{sp} at 550 nm wavelength and their simulated equivalents for different refractive indices.

The Nephelometer-measured σ_{sp} at 550 nm has the following statistics:

Minimum=13.3; Maximum=778.9; Mean =70.4; Median=53.3

(all expressed in Mm^{-1}).

Refr. Index	r	rmse[Mm^{-1}]
1.50-0.005i	0.943	22.4
1.50-0.01i	0.945	24.5
1.50-0.02i	0.947	29.3
1.55-0.005i	0.946	20.2
1.55-0.01i	0.948	22.3

Table 3

Correlation coefficients (r) between various Nephelometer-measured scattering coefficients and volumes of PCASP-measured fine (0.11-1.0 μm diameter) and coarse (1.0-3.3 μm diameter) size fractions.

Total/Back scatter	Wavelength [nm]	r (Fine)	r (Coarse)
Total	450	0.670	0.766
Total	550	0.566	0.866
Total	700	0.449	0.913
Back	450	0.418	0.780
Back	550	0.360	0.779
Back	700	0.319	0.774

Table 4

Coefficients of multivariate linear regression of scattering coefficients as a function of PCASP derived Fine and Coarse particle volumes. The wavelengths of the respective scattering/backscattering coefficients are indicated in parentheses. The a's are the multivariate regression coefficients, while the e's are their respective standard errors (all expressed in m^2/cm^3). R is the multiple coefficient of correlation.

	a_f	e_f	a_c	e_c	R
$\sigma_{sp}(450)$	13.114	0.235	0.958	0.014	0.901
$\sigma_{sp}(550)$	9.400	0.204	1.190	0.012	0.929
$\sigma_{sp}(700)$	5.576	0.195	1.319	0.011	0.934
$\sigma_{bsp}(450)$	1.061	0.060	0.205	0.003	0.806
$\sigma_{bsp}(550)$	0.768	0.063	0.214	0.004	0.793
$\sigma_{bsp}(700)$	0.516	0.060	0.203	0.003	0.781

Table 5

Coefficients of multivariate linear regression of scattering coefficients as a function of SFU-SNN derived Fine and Coarse particle masses. The wavelengths of the respective scattering/backscattering coefficients are indicated in parentheses. The a's are the multivariate regression coefficients, while the e's are their respective standard errors (all the expressed in m^2/g). R is the multiple coefficient of correlation.

	a_f	e_f	a_c	e_c	R
$\sigma_{sp}(450)$	5.099	0.679	-0.043	0.060	0.887
$\sigma_{sp}(550)$	3.669	0.567	0.121	0.050	0.921
$\sigma_{sp}(700)$	2.223	0.453	0.255	0.040	0.948
$\sigma_{bsp}(450)$	0.515	0.077	0.030	0.007	0.946
$\sigma_{bsp}(550)$	0.396	0.074	0.041	0.007	0.951
$\sigma_{bsp}(700)$	0.288	0.068	0.045	0.006	0.952

Table 6

Mutual correlation coefficients between Scattering Coefficients at 550 nm wavelength (Nephelometer) and Particle Mass, Black Carbon, and some major elements in the coarse and fine size fractions (SFU-SNN).

	σ_{sp}(550 nm)	Coarse_PM	Coarse_BC	Coarse_Na	Coarse_Al	Coarse_S	Coarse_Ca	Fine_PM	Fine_BC	Fine_Na	Fine_Al	Fine_S
σ_{sp}(550 nm)	1.00											
Coarse_PM	0.87	1.00										
Coarse_BC	0.80	0.77	1.00									
Coarse_Na	0.44	0.60	0.30	1.00								
Coarse_Al	0.88	0.99	0.81	0.55	1.00							
Coarse_S	0.89	0.92	0.89	0.50	0.94	1.00						
Coarse_Ca	0.82	0.98	0.68	0.63	0.94	0.85	1.00					
Fine_PM	0.82	0.69	0.71	0.33	0.65	0.66	0.70	1.00				
Fine_BC	0.11	-0.26	0.09	-0.47	-0.25	-0.11	-0.28	0.24	1.00			
Fine_Na	0.06	0.19	0.01	0.66	0.09	0.08	0.27	0.27	-0.26	1.00		
Fine_Al	0.80	0.84	0.91	0.41	0.86	0.84	0.77	0.74	-0.13	0.09	1.00	
Fine_S	-0.01	-0.38	-0.26	-0.26	-0.42	-0.31	-0.34	0.20	0.60	0.15	-0.39	1.00
Fine_Ca	0.72	0.88	0.67	0.58	0.81	0.74	0.92	0.80	-0.24	0.43	0.80	-0.24